Journal of Computational Physics 452 (2022) 110915

Contents lists available at ScienceDirect

Journal of Computational Physics

www.elsevier.com/locate/jcp

Efficient evaluation of three-dimensional Helmholtz Green's functions tailored to arbitrary rigid geometries for flow noise simulations

Stéphanie Chaillat [a], Benjamin Cotté [b], Jean-François Mercier [a,*], Gilles Serre [c], Nicolas Trafny [c]

[a] POEMS, CNRS-ENSTA-INRIA, Institut Polytechnique de Paris, France
[b] IMSIA, ENSTA-CNRS-CEA-EDF, Institut Polytechnique de Paris, France
[c] Naval Group, Naval Research, Ollioules, France

ARTICLE INFO

Article history:
Received 17 May 2021
Received in revised form 20 December 2021
Accepted 21 December 2021
Available online 3 January 2022

Keywords:
Tailored Green's functions
Fast BEMs
Helmholtz problems
Lighthill's equation

ABSTRACT

The Lighthill's wave equation provides an accurate characterization of the hydrodynamic noise due to the interaction between a turbulent flow and an obstacle, that is needed to get in many industrial applications. In the present study, to solve the Lighthill's equation expressed as a boundary integral equation, we develop an efficient numerical method to determine the three-dimensional Green's function of the Helmholtz equation in presence of an obstacle of arbitrary shape, satisfying a Neumann boundary condition. This so-called tailored Green's function is useful to reduce the computational costs to solve the Lighthill's equation. The first step consists in deriving an integral equation to express the tailored Green's function thanks to the free space Green's function. Then a Boundary Element Method (BEM) is used to compute tailored Green's functions. Furthermore, an efficient method is performed to compute the second derivatives needed for accurate flow noise determinations. The proposed approach is first tested on simple geometries for which analytical solutions can be determined (sphere, cylinder, half plane). In order to consider realistic geometries in a reasonable amount of time, fast BEMs are used: fast multipole accelerated BEM and hierarchical matrix based BEM. A discussion on the numerical efficiency and accuracy of these approaches in an industrial context is finally proposed.

1. Introduction

An accurate characterization of the noise radiation that appears when an obstacle is placed in a turbulent flow is necessary in many industrial applications. Depending mainly on the operating Mach number, different strategies have been developed. Naval applications we are primary interested in generally involve a low Mach number and a high Reynolds number which makes unsuitable direct noise computation methods. In this case, the most popular alternatives are acoustic analogies as introduced by Lighthill [1]. It consists in separating noise generation and noise propagation mechanisms. Lighthill's idea was to rewrite the fundamental equations of the fluid mechanics as a wave equation. It can then be solved

* Corresponding author.
E-mail address: jean-francois.mercier@ensta-paris.tex (J.-F. Mercier).

https://doi.org/10.1016/j.jcp.2021.110915
0021-9991/

either by using a finite element method or a boundary integral method for example. The finite element method would require to mesh a large computational domain and to introduce well-adapted boundary conditions on the artificial boundary introduced to truncate the computational domain. Since the boundary integral equation formalism satisfies intrinsically the Sommerfeld radiation condition at infinity, it should be the most suitable approach for far-field noise predictions in unbounded domains.

For any partial differential equation, various boundary integral equations can be derived. Among the possibilities, the choice of the boundary conditions satisfied by the Green's function is important since it enables to reduce the cost to evaluate the boundary integral representation. In our case, it can be mainly formulated by using the free-space Green's function or a tailored Green's function, which means that it satisfies the boundary condition over the obstacle, rigid for our case. The first use of a tailored Green's function in aeroacoustics was achieved by Doak [2] who showed that the computation of the total radiated field requires almost exclusively the knowledge of the Green's function satisfying the appropriate condition over the obstacle. In the solution using the tailored Green's function, two contributions to the total radiated field can be distinguished: a vibro-acoustic contribution and an aeroacoustic contribution. The former appears to be defined by the value of the tailored Green's function over the obstacle surface and the latter by the second derivatives of the tailored Green function inside the turbulence volume see forthcoming Eq. (6). These second derivatives are characteristic of the noise amplification due to the nearfield flow scattering by the obstacle geometry [3]. Since then, most applications involving tailored Green's functions are dimensional analysis [4]. However, during the last decade analytical tailored Green's functions have been successfully applied to roughness noise prediction [5]. However they are derived for the particular geometries, step [5] or hemispheres [6] and they cannot be extended to a finite size more general geometry or a curved geometry for instance.

The determination of the tailored Green's function can be achieved analytically for canonical geometries but must be done numerically for geometries of arbitrary shapes. Boley [7] initially proposed in 1956 to compute the exact Green's function, defined as a solution of the Helmholtz equation, with a boundary integral equation. The only applications in aeroacoustics of a numerical three-dimensional Green's function date to the work of Ostertag et al. [8] in 2000, of Hu [9] in 2005 and of Takaishi [10] 2007. In these works, the numerical method is not thoroughly described and a standard BEM (not accelerated) is used. In this work, we propose to take advantage of the recent improvements of the capabilities of BEMs to propose an efficient procedure for the computation of the tailored Green's function in the context of aeroacoustic prediction models at low Mach number.

This paper is organized as follows. In Section 2, we recall classical works on the resolution of Lighthill's equation and show the advantages obtained by using the tailored Green's function. In Section 3, we derive the tailored Green's function and its spatial second derivatives with a boundary integral representation. In particular a semi-analytical strategy is developed to determine accurately the second derivatives. In Section 4, we discuss the efficient numerical evaluation of these special Green's functions with two recent acceleration methods: the fast multipole method and hierarchical matrices. In Section 5 the approach is validated on simple geometries for which analytical solutions can be determined (sphere, cylinder, half plane). A discussion on the numerical efficiency and accuracy of the fast approach in an industrial context is finally proposed in Section 6.

2. Evaluating the integral solution of Lighthill's pressure

We consider a bounded obstacle $\mathcal{O}$ of boundary Γ. We note $\Omega = \mathbb{R}^3 \backslash \mathcal{O}$ the exterior of the obstacle. The Lighthill's wave equation [1] determines the sound emitted by the flow around the obstacle $\mathcal{O}$. In the time-harmonic regime with frequency ω ($e^{-i\omega t}$ dependence), the Lighthill's equation is:

$$\left\{ \begin{array}{rcl} -\Delta p' - k_0^2 p' & = & \dfrac{\partial^2 T_{ij}}{\partial x_i \partial x_j} \quad \text{in } \Omega, \\ \text{where } T_{ij} & = & \rho v_i v_j + p_{ij} - p' \delta_{ij}, \end{array} \right.$$

where we do not precise for the moment the boundary condition on the obstacle. $p' = p - p_\infty$ is the pressure perturbation relative to the surrounding medium where p is the fluid pressure and p_∞ is the surrounding ambient pressure. $\boldsymbol{v}$ is the fluid velocity and ρ the density. We have introduced the wavenumber $k_0 = \omega / c_\infty$ with c_∞ the sound speed. $p_{ij} = p' \delta_{ij} - \sigma_{ij}$ is the compressive stress tensor with σ_{ij} the viscous stress tensor. T_{ij} is Lighthill's stress tensor. It is frequently referred to as a source term because it contains all the effects that generate acoustic waves, including propagations effects (convection and refraction) and we also consider in this work that we have access to this source term T_{ij}.

A solution to Lighthill's wave equation can be obtained by using the method of Green's functions combined with Curle's theorem. For an arbitrary Green's function $\tilde{G}$, the Lighthill pressure p' satisfies $\forall \boldsymbol{x} \in \Omega$ the integral representation [11]

$$p'(\boldsymbol{x}) = \int_\Omega T_{ij}(\boldsymbol{y}) \frac{\partial^2 \tilde{G}}{\partial y_i \partial y_j}(\boldsymbol{x}, \boldsymbol{y}) d\boldsymbol{y} + \int_\Gamma \left[(p_{ij} + \rho v_i v_j)(\mathbf{Y}) \frac{\partial \tilde{G}}{\partial Y_i}(\boldsymbol{x}, \mathbf{Y}) - i\omega \tilde{G}(\boldsymbol{x}, \mathbf{Y}) \rho v_j(\mathbf{Y}) \right] n_j(\mathbf{Y}) dS_{\mathbf{Y}}, \tag{1}$$

with $\boldsymbol{n}$ the normal pointing outward $\mathcal{O}$ (thus inward Ω).

To get the second integral in (1), the momentum equation

$$-i\omega(\rho v_i) + \frac{\partial}{\partial x_j}(\rho v_i v_j + p_{ij}) = 0,$$

has been used. Then, once it is combined with the definition of T_{ij}, it leads to

$$\frac{\partial}{\partial x_j}(T_{ij} + p'\delta_{ij}) = i\omega(\rho v_i),$$

and thus to the second integral in (1) since $v_i n_i = v_j n_j$. From now we use a simple convention to differentiate points in Ω from points on Γ: small letters for coordinates in Ω and capital letters for coordinates on Γ. We introduce two simplifications: we consider that the velocity of the boundary Γ is small and thus we neglect the term $v_i v_j$ in T_{ij} on Γ. Moreover for high Reynolds number flow we can neglect the viscous stress such that $p_{ij} = p'\delta_{ij}$. With these hypotheses, the boundary integral representation reduces to

$$p'(\boldsymbol{x}) = \int_\Omega T_{ij}(\boldsymbol{y})\frac{\partial^2 \tilde{G}}{\partial y_i \partial y_j}(\boldsymbol{x},\boldsymbol{y})d\boldsymbol{y} + \int_\Gamma \left[p'(\mathbf{Y})\frac{\partial \tilde{G}}{\partial \mathbf{Y}_j}(\boldsymbol{x},\mathbf{Y})n_j(\mathbf{Y}) - i\omega\rho v_j(\mathbf{Y})n_j(\mathbf{Y})\tilde{G}(\boldsymbol{x},\mathbf{Y})\right] dS_{\mathbf{Y}}. \tag{2}$$

The simplest choice for $\tilde{G}$ is the free field Green's function, i.e., $\tilde{G} = G_0$. It is defined for a fixed source localized at $\boldsymbol{y} \in \Omega$ by

$$(\Delta_{\boldsymbol{z}} + k_0^2)G_0(\boldsymbol{y},\boldsymbol{z}) + \delta(\boldsymbol{y}-\boldsymbol{z}) = 0 \quad \forall \boldsymbol{z} \in \mathbb{R}^3, \tag{3}$$

such that

$$G_0(\boldsymbol{y},\boldsymbol{z}) = \frac{e^{ik_0|\boldsymbol{y}-\boldsymbol{z}|}}{4\pi|\boldsymbol{y}-\boldsymbol{z}|}. \tag{4}$$

However, it is not a clever choice because it would require to first determine p' on the boundary Γ to be able to apply the boundary integral representation (2). This first step would require to solve a problem similar to a boundary integral equation for p' on Γ. But although boundary integral equations are efficient in the absence of a source term, the solution of this integral equation would be particularly expensive due to the presence of a volume term (first term in (2)).

An alternative and more suitable choice is to use a special Green's function to avoid the need of determining p' on Γ for each source. Such function will be called the **tailored Green's function** and it is denoted G_T. This tailored function is independent from the flow, dependent only from surface geometries and boundary conditions, in our case a rigid boundary condition on Γ. It is thus solution, for a fixed source localized at $\boldsymbol{x} \in \Omega$, of

$$\begin{cases} (\Delta_{\boldsymbol{z}} + k_0^2)G_T(\boldsymbol{x},\boldsymbol{z}) + \delta(\boldsymbol{x}-\boldsymbol{z}) &= 0 \quad \forall \boldsymbol{z} \in \Omega, \\ \partial_{\boldsymbol{n_z}} G_T(\boldsymbol{x},\mathbf{Z}) &= 0 \quad \forall \mathbf{Z} \in \Gamma, \end{cases} \tag{5}$$

where the normal derivative $\partial_{\boldsymbol{n_z}} G_T(\boldsymbol{x},\mathbf{Z})$ stands for $\boldsymbol{n}\cdot\nabla_{\mathbf{Z}} G_T(\boldsymbol{x},\mathbf{Z}) = \sum_{i=1}^{3} n_i \frac{\partial G_T}{\partial Z_i}(\boldsymbol{x},\mathbf{Z})$. With this choice of Green's function, the integral representation (1) simplifies for all $\boldsymbol{x} \in \Omega$ in

$$p'(\boldsymbol{x}) = \int_\Omega T_{ij}(\boldsymbol{y})\frac{\partial^2 G_T}{\partial y_i \partial y_j}(\boldsymbol{x},\boldsymbol{y})d\boldsymbol{y} - i\omega\int_\Gamma G_T(\boldsymbol{x},\mathbf{Y})\,(\rho\boldsymbol{v}\cdot\boldsymbol{n})(\mathbf{Y})dS_{\mathbf{Y}}. \tag{6}$$

This new integral representation highlights two advantages to use the tailored Green's function. First, once the source terms T_{ij} and $\boldsymbol{v}\cdot\boldsymbol{n}$ are known, p' in (6) can be easily computed. There is no integral equation to solve. Moreover the tailored Green's function has a physical meaning. It appears that the directivity of the tailored Green's function, obtained by plotting $G_T(\boldsymbol{x},\boldsymbol{y})$ for a fixed $\boldsymbol{y}$ and a moving $\boldsymbol{x}$, is similar to the directivity of the Lighthill's solution p'. For instance, for a rigid boundary $\boldsymbol{v}\cdot\boldsymbol{n} = 0$ by using the mean value theorem we have

$$p'(\boldsymbol{x}) = \int_\Omega T_{ij}(\boldsymbol{y})\frac{\partial^2 G_T}{\partial y_i \partial y_j}(\boldsymbol{x},\boldsymbol{y})d\boldsymbol{y} = |\Omega| T_{ij}(\boldsymbol{y}_0(\boldsymbol{x}))\frac{\partial^2 G_T}{\partial y_i \partial y_j}(\boldsymbol{x},\boldsymbol{y}_0(\boldsymbol{x})),$$

where $\boldsymbol{y}_0(\boldsymbol{x})$ is a particular point in Ω and $|\Omega|$ is the volume of Ω. Therefore $p'(\boldsymbol{x})$ has the same variations as $\partial^2 G_T/\partial y_i \partial y_j(\boldsymbol{x},\boldsymbol{y}_0(\boldsymbol{x}))$ when $\boldsymbol{x}$ moves, in particular if the support of T_{ij} is small (then $\boldsymbol{y}_0(\boldsymbol{x})$ can be considered fixed).

3. Procedure to determine the tailored Green's function

Since no analytical expression of G_T is available in presence of complex geometries, the originality of this work is to evaluate efficiently $G_T(\boldsymbol{x},\boldsymbol{y})$ for all $\boldsymbol{x},\boldsymbol{y} \in \Omega$ by using existing techniques developed for fast Boundary Element Methods formulated with G_0. The first step is to express the boundary integral equation satisfied by G_T.

3.1. Derivation of the Boundary Integral Representation for the tailored Green's function

We start by deriving the integral representation for the tailored Green's function G_T.

Lemma 3.1. *For a fixed source localized at $\boldsymbol{y} \in \Omega$ and for all observation points $\boldsymbol{x} \in \Omega$, the integral representation of the tailored Green's function $G_T(\boldsymbol{x}, \boldsymbol{y})$ solution of (5) is given by*

$$G_T(\boldsymbol{x}, \boldsymbol{y}) - G_0(\boldsymbol{x}, \boldsymbol{y}) = \int_\Gamma \partial_{\boldsymbol{n_z}} G_0(\boldsymbol{y}, \mathbf{Z}) G_T(\boldsymbol{x}, \mathbf{Z}) dS_{\mathbf{Z}}, \tag{7}$$

with

$$\partial_{\boldsymbol{n_z}} G_0(\boldsymbol{y}, \mathbf{Z}) = (\mathbf{Z} - \boldsymbol{y}) \cdot \boldsymbol{n}(\mathbf{Z}) \frac{ik_0|\mathbf{Z} - \boldsymbol{y}| - 1}{|\mathbf{Z} - \boldsymbol{y}|^3} \frac{e^{ik_0|\mathbf{Z}-\boldsymbol{y}|}}{4\pi}. \tag{8}$$

Proof. For all $\boldsymbol{x}, \boldsymbol{y} \in \Omega$, multiplying (3) by $G_T(\boldsymbol{x}, \boldsymbol{z})$ and (5) by $G_0(\boldsymbol{y}, \boldsymbol{z})$, substracting the two terms and integrating on all $\boldsymbol{z} \in \Omega$ leads to [11,12]

$$G_T(\boldsymbol{x}, \boldsymbol{y}) - G_0(\boldsymbol{y}, \boldsymbol{x}) + \int_\Omega G_T(\boldsymbol{x}, \boldsymbol{z})(\Delta_{\boldsymbol{z}} + k_0^2) G_0(\boldsymbol{y}, \boldsymbol{z}) d\boldsymbol{z} - \int_\Omega G_0(\boldsymbol{y}, \boldsymbol{z})(\Delta_{\boldsymbol{z}} + k_0^2) G_T(\boldsymbol{x}, \boldsymbol{z}) d\boldsymbol{z} = 0.$$

Noting $\boldsymbol{m}$ the normal on Γ pointing outward Ω, we get

$$G_T(\boldsymbol{x}, \boldsymbol{y}) - G_0(\boldsymbol{y}, \boldsymbol{x}) + \int_\Gamma \partial_{\boldsymbol{m_z}} G_0(\boldsymbol{y}, \mathbf{Z}) G_T(\boldsymbol{x}, \mathbf{Z}) dS_{\mathbf{Z}} - \int_\Gamma \partial_{\boldsymbol{m_z}} G_T(\boldsymbol{x}, \mathbf{Z}) G_0(\boldsymbol{y}, \mathbf{Z}) dS_{\mathbf{Z}} = 0.$$

Using the rigid boundary condition on Γ and the reciprocity $G_0(\boldsymbol{y}, \boldsymbol{x}) = G_0(\boldsymbol{x}, \boldsymbol{y})$, it leads to

$$G_T(\boldsymbol{x}, \boldsymbol{y}) - G_0(\boldsymbol{x}, \boldsymbol{y}) + \int_\Gamma \partial_{\boldsymbol{m_z}} G_0(\boldsymbol{y}, \mathbf{Z}) G_T(\boldsymbol{x}, \mathbf{Z}) dS_{\mathbf{Z}} = 0.$$

Eventually, since $\boldsymbol{n} = -\boldsymbol{m}$ is the natural normal pointing outward $\mathcal{O}$, we get the result, which is also formula (4.6.1) of [11]. □

The integral representation (7) indicates that the only remaining unknown is $G_T(\boldsymbol{x}, \mathbf{Z})$ for all $\mathbf{Z} \in \Gamma$. To determine $G_T(\boldsymbol{x}, \mathbf{Z})$, we introduce some classical integral operators: the single and double layer potentials, which to a function $\phi(\mathbf{Z})$ defined for $\mathbf{Z} \in \Gamma$ associate the functions defined for any $\boldsymbol{y} \in \Omega$ by

$$(\mathcal{S}\phi)(\boldsymbol{y}) = \int_\Gamma G_0(\boldsymbol{y}, \mathbf{Z}) \phi(\mathbf{Z}) dS_{\mathbf{Z}}, \quad (\mathcal{D}\phi)(\boldsymbol{y}) = \int_\Gamma \partial_{n_{\mathbf{Z}}} G_0(\boldsymbol{y}, \mathbf{Z}) \phi(\mathbf{Z}) dS_{\mathbf{Z}}. \tag{9}$$

To simplify the notations, for a fixed $\boldsymbol{x} \in \Omega$, we set $G_T^{\boldsymbol{x}}(\boldsymbol{y}) = G_T(\boldsymbol{x}, \boldsymbol{y})$ and $G_0^{\boldsymbol{x}}(\boldsymbol{y}) = G_0(\boldsymbol{x}, \boldsymbol{y})$, we get

$$(\mathcal{D}G_T^{\boldsymbol{x}})(\boldsymbol{y}) = \int_\Gamma \partial_{n_{\mathbf{Z}}} G_0^{\boldsymbol{y}}(\mathbf{Z}) G_T^{\boldsymbol{x}}(\mathbf{Z}) dS_{\mathbf{Z}} = \int_\Gamma \partial_{n_{\mathbf{Z}}} G_0(\boldsymbol{y}, \mathbf{Z}) G_T(\boldsymbol{x}, \mathbf{Z}) dS_{\mathbf{Z}}.$$

Then (7) becomes

$$\boxed{G_T^{\boldsymbol{x}}(\boldsymbol{y}) - G_0^{\boldsymbol{x}}(\boldsymbol{y}) = (\mathcal{D}G_T^{\boldsymbol{x}})(\boldsymbol{y}), \quad \forall \boldsymbol{y} \in \Omega \text{ and a fixed } \boldsymbol{x} \in \Omega} \tag{10}$$

To determine $G_T^{\boldsymbol{x}}(\boldsymbol{y})$ for all $\boldsymbol{y} \in \Omega$ thanks to (10), we just need to determine $G_T^{\boldsymbol{x}}(\mathbf{Y})$ for $\mathbf{Y} \in \Gamma$ and this is done thanks to an integral equation, derived in the following section.

3.2. Derivation of the Boundary Integral Equation governing the tailored Green's function

The Dirichlet trace operator γ_0^+ associates to a function $\varphi(\boldsymbol{y})$ with $\boldsymbol{y} \in \Omega$ the trace on Γ, i.e., the function $(\gamma_0^+ \varphi)(\mathbf{Y})$ with $\mathbf{Y} \in \Gamma$, defined by $\lim_{\boldsymbol{y} \to \mathbf{Y}} \varphi(\boldsymbol{y})$. It is known [13] that the traces of the operators in (9) are given by

$$\gamma_0^+ \mathcal{S} = S, \quad \gamma_0^+ \mathcal{D} = \frac{I}{2} + D,$$

where we have introduced the boundary operators defined for $\mathbf{Y} \in \Gamma$ by

$$(S\phi)(\mathbf{Y}) = \int_\Gamma G_0^{\mathbf{Y}}(\mathbf{Z})\phi(\mathbf{Z})dS_{\mathbf{Z}}, \tag{11}$$

$$(D\phi)(\mathbf{Y}) = \int_\Gamma \partial_{n_{\mathbf{Z}}} G_0^{\mathbf{Y}}(\mathbf{Z})\phi(\mathbf{Z})dS_{\mathbf{Z}}. \tag{12}$$

Due to the singularity of $G_0^{\mathbf{Y}}(\mathbf{Z})$ at $\mathbf{Z} = \mathbf{Y}$, for D the integral on Γ has to be understood as a principal value. Using these results on the traces, the integral equation is given by the following lemma.

Lemma 3.2. *For any $\boldsymbol{x} \in \Omega$ and all $\mathbf{Y} \in \Gamma$, the tailored Green's function $G_T^{\boldsymbol{x}}$ is solution of the following boundary integral equation*

$$\left[\left(\frac{I}{2} - D\right) G_T^{\boldsymbol{x}}\right](\mathbf{Y}) = G_0^{\boldsymbol{x}}(\mathbf{Y}). \tag{13}$$

Proof. For a fixed $\boldsymbol{x} \in \Omega$, taking the Dirichlet trace γ_0^+ of (10), we obtain $\forall \mathbf{Y} \in \Gamma$

$$G_T^{\boldsymbol{x}}(\mathbf{Y}) - G_0^{\boldsymbol{x}}(\mathbf{Y}) = \left[\left(\frac{I}{2} + D\right) G_T^{\boldsymbol{x}}\right](\mathbf{Y}).$$

(13) is obtained straightforwardly. Note that it is also formula (4.6.3) of [11].

□

4. Numerical determination of the tailored Green's function

To evaluate p' for all $\boldsymbol{x} \in \Omega$ with the boundary integral representation (6), it is first required to determine $G_T^{\boldsymbol{x}}(\boldsymbol{y})$. We follow the classical steps of the Boundary Element Method (BEM). It is decomposed into two steps: the trace, i.e., $G_T^{\boldsymbol{x}}(\mathbf{Y})$, is determined on the boundary Γ and then the integral representation is invoked to obtain the values in the volume, i.e., for a fixed $\boldsymbol{x} \in \Omega$:

- Step 1: solve the boundary integral equation (13) to obtain $G_T^{\boldsymbol{x}}(\mathbf{Y})$ for all $\mathbf{Y} \in \Gamma$,
- Step 2: invoke the boundary integral representation (10) (or equivalently (7)) for all the wanted $\boldsymbol{y} \in \Omega$.

4.1. Cost of the standard (non-accelerated) method

Let us evaluate the cost of the determination of $G_T^{\boldsymbol{x}}(\boldsymbol{y})$ for a fixed point $\boldsymbol{x} \in \Omega$. We introduce the following notations: N_v corresponds to the number of discretization points in the volume Ω. N_b corresponds to the number of discretization points on the boundary Γ.

Costs to determine $G_T^{\boldsymbol{x}}(\mathbf{Y})$ and $G_T^{\boldsymbol{x}}(\boldsymbol{y})$ The main cost in this procedure comes from the first step. Hence, for a fixed $\boldsymbol{x}$, the vector $G_T^{\boldsymbol{x}}(\mathbf{Y})$ of size N_b (for all the points $\mathbf{Y}$ on Γ) is obtained by solving a fully populated system of size $N_b \times N_b$. Its cost is thus of the order of $\mathcal{O}(N_b^2)$ if an iterative solver is used, e.g., GMRES. The second step to compute $G_T^{\boldsymbol{x}}(\boldsymbol{y})$ for all wanted $\boldsymbol{y} \in \Omega$ reduces to a matrix-vector product in (10) with a cost of the order of $\mathcal{O}(N_b N_v)$. Therefore the cost of the overall procedure is finally given by $\mathcal{O}(N_b(N_b + N_v))$.

Cost to determine the pressure p' Now we determine the cost to evaluate the integral representation (6) in Ω. It contains two terms. The second term is an integral over the surface Γ. Once the Green's function $G_T^{\boldsymbol{x}}(\mathbf{Y})$ has been obtained with a cost of $\mathcal{O}(N_b^2)$, if we know the velocity on the boundary Γ, the evaluation of the integral is of order $\mathcal{O}(N_b)$. Therefore the total cost for this term is $\mathcal{O}(N_b(N_b+1))$. The first term is more complex and requires to evaluate the second derivative of the tailored Green's function. A naive method would be to use a finite differences formula: for instance for a cartesian grid and for any small real Δy, we could use the following four-points approximation

$$\frac{\partial^2 G_T}{\partial y_i \partial y_j}(\boldsymbol{x}, \boldsymbol{y}) \simeq \frac{G_T(\boldsymbol{x} + \Delta y(\boldsymbol{e}_i + \boldsymbol{e}_j), \boldsymbol{y}) - G_T(\boldsymbol{x} + \Delta y(\boldsymbol{e}_i - \boldsymbol{e}_j), \boldsymbol{y}) + G_T(\boldsymbol{x} - \Delta y(\boldsymbol{e}_i + \boldsymbol{e}_j), \boldsymbol{y}) - G_T(\boldsymbol{x} - \Delta y(\boldsymbol{e}_i - \boldsymbol{e}_j), \boldsymbol{y})}{(2\Delta y)^2},$$

where $(\boldsymbol{e}_1, \boldsymbol{e}_2, \boldsymbol{e}_3)$ is the $\mathbb{R}^3$-basis. A drawback of this interpolation approach is that it requires four evaluations of $G_T(\boldsymbol{x}, \boldsymbol{y})$ and that it is valid only for a structured mesh. Since structured meshes are not suitable for complex geometry, we propose instead to use the capability of boundary integral equations to obtain this term in a faster and more accurate way. A semi-analytical strategy is developed: by derivating (7): since G_T in the integral is not derived, we directly have access to the derivative by evaluating

$$\frac{\partial^2 G_T}{\partial y_i \partial y_j}(\boldsymbol{x},\boldsymbol{y}) = \frac{\partial^2 G_0}{\partial y_i \partial y_j}(\boldsymbol{x},\boldsymbol{y}) + \int_\Gamma \partial_{\boldsymbol{n_Z}} \frac{\partial^2 G_0}{\partial y_i \partial y_j}(\boldsymbol{y},\mathbf{Z})\, G_T(\boldsymbol{x},\mathbf{Z})\, dS_{\mathbf{Z}}. \tag{14}$$

Since $\partial^2 G_0/\partial y_i \partial y_j$ is known explicitly (see Appendix C), the cost is the same as for the calculation of $G_T(\boldsymbol{x},\boldsymbol{y})$, thus of order $\mathcal{O}(N_b(N_b+N_v))$. Step 1 is not modified to obtain $G_T(\boldsymbol{x},\mathbf{Z})$ for all $\mathbf{Z}\in\Gamma$ and in Step 2 the integral representation (14) is invoked instead of (10). Finally to determine p', a volume integral where $\boldsymbol{y}$ spans the volume Ω for a fixed $\boldsymbol{x}\in\Omega$, remains to be determined, with a cost of $\mathcal{O}(N_v)$. Therefore the evaluation of this volume integral is of the order of $\mathcal{O}(N_b(N_b+N_v)+N_v)$.

We understand at this point the limitation of standard approaches. With a computational cost increasing quadratically with the number of points on the boundary, it is problematic to use this method in realistic configurations.

4.2. Speeding up the numerical solution with fast BEM

The main computational cost in our approach is due to the solution of the boundary integral equation with standard Boundary Element Methods. We refer to [16] for a complete introduction to the method. Importantly, the discretization process of the BEM transforms (13) into a square complex-valued linear system of size N_b of the form

$$\mathbb{A}\mathbf{G}^x = \mathbf{b}, \tag{15}$$

where the (N_b)-vector $\mathbf{G}^x$ collects the degrees of freedom (DOFs) while the (N_b)-vector $\mathbf{b}$ arises from the imposed right-hand side. Assembling the full dense matrix $\mathbb{A}$ requires the computation of all element integrals at each collocation point, thus requiring an $\mathcal{O}(N_b^2)$ computational time and memory. If an iterative method is used, each GMRES iteration requires one evaluation of $\mathbb{A}\mathbf{G}^x$ for a given $\mathbf{G}^x$, a task requiring a computing time of order $\mathcal{O}(N_b^2)$. Obviously it is the most accurate BEM but at the price of prohibitive computational costs to consider realistic geometries. It will only be used as a numerical reference solution in the following and it will be called the standard BEM. To lower the $\mathcal{O}(N_b^2)$ complexity, prohibitive for large BEM models, we use the capabilities offered by fast BEMs. The two main approaches to speed-up the BEM are the Fast Multipole accelerated BEM (FM-BEM) and the Hierarchical matrix based BEM ($\mathcal{H}$-BEMs). Since these two approaches have complementary advantages and drawbacks, we will consider both of them to give a clear overview of their domains of interest.

The goal of a FMM (Fast Multipole Method) [14,17] is to accelerate the evaluation of the matrix-vector product $\mathbb{A}\mathbf{q}$ for a given $\mathbf{q}$, required at each iteration of an iterative solver applied to the BEM-discretized equations. Another advantage of the method is that the governing BEM matrix is never explicitly formed, which leads to a storage requirement well below $\mathcal{O}(N_b^2)$. In general terms, the FMM exploits an analytical (plane wave based) expansion of the full-space Green's function in terms of products of functions of $\mathbf{X}$ and of $\mathbf{Y}$, so that (unlike in the standard BEM) integrations with respect to $\mathbf{Y}$ can be reused when the collocation point $\mathbf{X}$ is changed. Since it is based on an analytical expansion, it has been shown numerically and theoretically to be the most efficient accelerated BEM for oscillatory problems with a complexity of $\mathcal{O}(N_b \log N_b)$ per GMRES iteration. However, this optimal complexity is obtained for a uniform discretization of the domain boundary, i.e., if the mesh size is tailored to the geometry. To sum up, this approach is expected to be efficient for mid to high frequency problems for which the mesh is not over-refined with respect to the frequency of the problem.

An alternative approach to speed-up the BEM is to use a data-sparse representation of the system matrix. Hierarchical matrices or $\mathcal{H}$-matrices have been introduced by Hackbusch [15]. The principle of $\mathcal{H}$-matrices is (i) to partition the matrix into blocks and (ii) to perform low-rank approximations of the blocks of the matrix which are known *a priori* (by using an admissibility condition) to be accurately approximated by low-rank decompositions [19]. Using low-rank representations, the memory requirements and costs of a matrix-vector product are reduced. Contrary to the FMM, it is an algebraic approach only based on an a priori knowledge on the relation between the matrix entries and the discretization of the geometry. Thus the configurations for which it gives its best results in terms of efficiency differ from the FMM. More precisely, it has been shown in [18] that this method is more efficient in the low frequency regime and when the discretization is over-refined; with a complexity of $\mathcal{O}(N_b \log N_b)$ if the number of degrees of freedom increases while the frequency is fixed.

To the authors' best knowledge, these considerations have never been checked on the same examples. In this work, in addition to check the efficiency of these three methods to evaluate tailored Green's functions, we will show the most appropriate regime of application of them. All of these methods are available in the code COFFEE developed at POEMS.[1] It will be used in the following numerical illustrations.

5. Numerical validation for geometries with known analytical Green's functions

In this Section, we check numerically the performances of the two steps detailed in paragraph 4 to determine the tailored Green's function: step 1 to solve (13) and step 2 to evaluate (10). To quantify the accuracy of these two steps, we compare

[1] https://uma.ensta-paris.fr/soft/COFFEE/.

the numerical results to explicit expressions of the tailored Green's function. These solutions are available only for simple geometries: a sphere, an infinite cylinder and a semi-infinite thin plate. In all the validation tests, we consider a source localized at $\boldsymbol{y} = (y_1, y_2, y_3)$ and an observation point at $\boldsymbol{x} = (x_1, x_2, x_3)$, i.e., $\boldsymbol{x}$ and $\boldsymbol{y}$ in Ω.

5.1. Validation for a sphere

We consider a sphere of radius R and we introduce the spherical coordinates: $\boldsymbol{x}$ is parametrized by $(r_x, \theta_x, \varphi_x)$ with $r_x^2 = x_1^2 + x_2^2 + x_3^2$ and $\boldsymbol{x} = r_x(\sin\theta_x \cos\varphi_x, \sin\theta_x \sin\varphi_x, \cos\theta_x)$. Similarly, we have $\boldsymbol{y} = r_y(\sin\theta_y \cos\varphi_y, \sin\theta_y \sin\varphi_y, \cos\theta_y)$ with $r_y^2 = y_1^2 + y_2^2 + y_3^2$.

5.1.1. Exact Green's function for a sphere

For $r_x > r_y$ the Green's function is given by [20]

$$G_T(\boldsymbol{x}, \boldsymbol{y}) = \frac{ik_0}{4\pi} \sum_{n=0}^{\infty} (2n+1) h_n(k_0 r_x) \left[j_n(k_0 r_y) - \alpha_n(k_0 R) h_n(k_0 r_y) \right] \times \left[\sum_{m=0}^{\infty} \epsilon_m \frac{(n-m)!}{(n+m)!} \cos\left[m(\varphi_x - \varphi_y) \right] P_n^m(\cos\theta_x) P_n^m(\cos\theta_y) \right], \tag{16}$$

where $\alpha_n(u) = \dfrac{j_n'(u)}{h_n'(u)}$. We have introduced $f_n(x) = \sqrt{\dfrac{\pi}{2x}} F_{n+\frac{1}{2}}(x)$ where $f = j$ or h (and $F = J$ or H), satisfying $(2n+1) f_n' = n f_{n-1} - (n+1) f_{n+1}$. j and h are the spherical Bessel and Hankel functions whereas J and H are the cylindrical Bessel and Hankel functions.

5.1.2. Trace of the Green's function on the boundary of the sphere

For the numerical results, the $\mathcal{H}$-BEM is used and the problem size is set to 12 620 DOFs with a largest mesh size of $L_{\max} = 50\,\text{mm}$. In the first step, we solve the boundary integral equation (13) to obtain the tailored Green's function $G_T^{\boldsymbol{x}}(\mathbf{Y}) = G_T(\boldsymbol{x}, \mathbf{Y})$ on the sphere $R = 1\,\text{m}$ for a fixed observation point at $\boldsymbol{x} = (100\,\text{m}, 0, 0)$ and a varying source on the sphere in the plane $Y_3 = 0$, thus with $r_Y = 1\,\text{m}$ and $\theta_Y = \pi/2$: $\mathbf{Y} = (\cos\varphi_Y, \sin\varphi_Y, 0)$.

In Fig. 1 we represent the modulus and argument of the relative Green's function

$$G_S = G_T - G_0,$$

with respect to φ_Y for $k_0 = 2\pi/3\,\text{m}^{-1}$ and $k_0 = 6\pi\,\text{m}^{-1}$, and we compare the numerical and analytical solutions. They are found in very good agreement. Of course the agreement cannot be perfect because of the numerical truncation.

5.1.3. Green's function for a fixed observation point and an arc of sources

Now we check the Step 2 by locating the source out of the sphere. From Step 1, we have $G_T(\boldsymbol{x}, \mathbf{Y})$ for all $\mathbf{Y}$ on the sphere and we are able to determine $G_S(\boldsymbol{x}, \boldsymbol{y})$ for any $\boldsymbol{y}$ outside of the sphere by using the boundary integral representation (7):

$$G_S(\boldsymbol{x}, \boldsymbol{y}) = \int_\Gamma \partial_{\boldsymbol{n}_\mathbf{Z}} G_0(\boldsymbol{y}, \mathbf{Z}) G_T(\boldsymbol{x}, \mathbf{Z}) dS_\mathbf{Z}.$$

The source is chosen now to move on the circle of radius $r_y = 1.1\,\text{m}$ in the plane $y_3 = 0$, again with the fixed observation point at $\boldsymbol{x} = (100\,\text{m}, 0, 0)$. Therefore we plot $f(\varphi_y) = G_S(\boldsymbol{x}, r_y(\cos\varphi_y, \sin\varphi_y, 0))$ in Fig. 2. From (16), the exact solution is

$$f(\varphi_y) = \frac{ik_0}{4\pi} \sum_{n=0}^{\infty} (2n+1) h_n(k_0 r_x) \left[j_n(k_0 r_y) - \alpha_n(k_0 R) h_n(k_0 r_y) \right] \times, \left[\sum_{m=0}^{\infty} \epsilon_m \frac{(n-m)!}{(n+m)!} \cos\left(m\varphi_y \right) P_n^m(0) P_n^m(0) \right]. \tag{17}$$

The agreement between the numerical and analytical solutions is again good. Importantly, this evaluation is fast since $G_T(\boldsymbol{x}, \mathbf{Z})$ is already stored for all $\mathbf{Z}$ on the sphere. It reduces to the evaluation of a matrix-vector product.

5.1.4. Green's function for a fixed source point and an arc of observation points

Here we still check the Step 2, the observation point $\boldsymbol{x}$ is again far from the sphere but it is no longer fixed, it moves on the circle of radius $r_x = 100\,\text{m}$ in the plane $x_3 = 0$. The source is now fixed at $\boldsymbol{y} = (1.1\,\text{m}, 0, 0)$. We consider again the solution of (7) and plot $g(\varphi_x) = G_S(r_x(\cos\varphi_x, \sin\varphi_x, 0), \boldsymbol{y})$ in Fig. 3. From (16), the analytical function g is given by

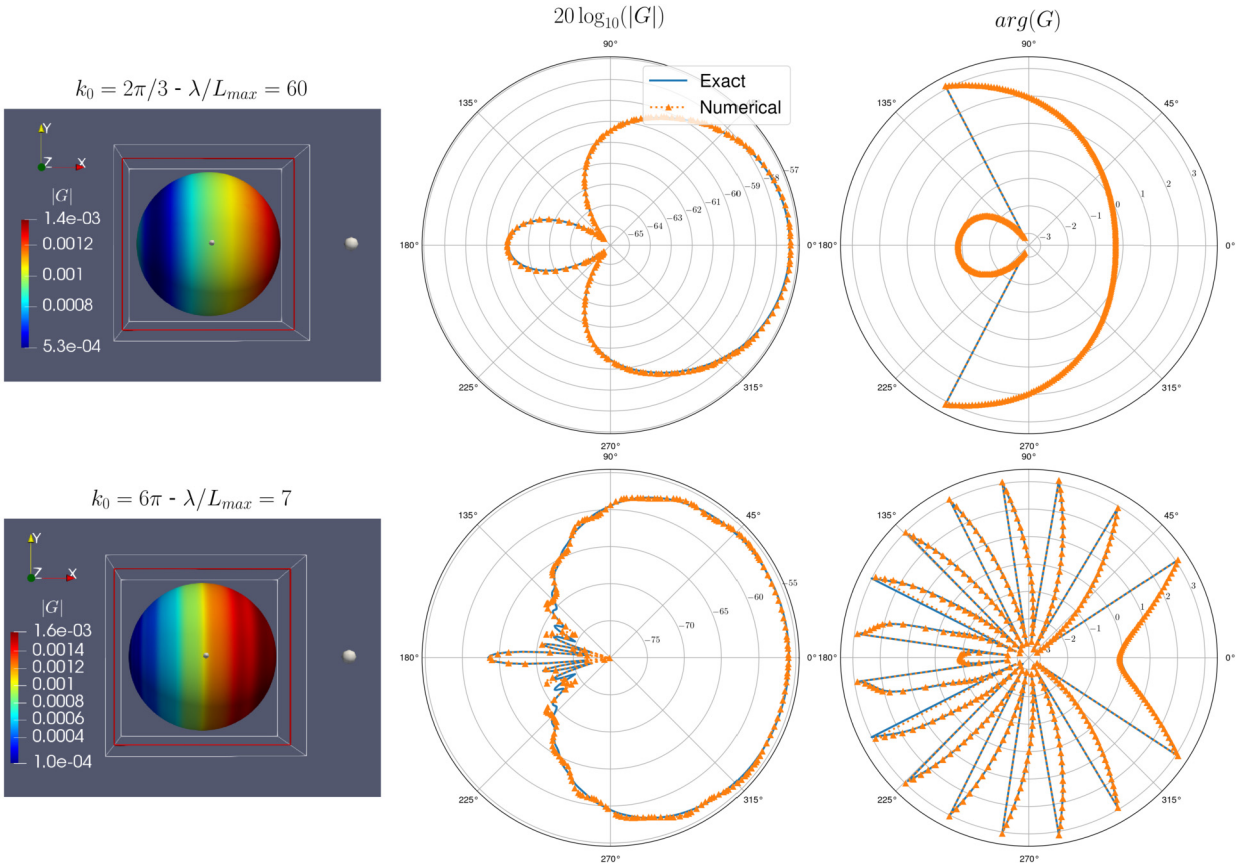

Fig. 1. Relative Green's function $G_S(\boldsymbol{x}, \mathbf{Y})$ for a sphere of radius $R = 1\,\mathrm{m}$ for a fixed observation point at $\boldsymbol{x} = (100\,\mathrm{m}, 0, 0)$ and a varying source on the sphere in the plane $Y_3 = 0$. Comparison between the numerical and analytical solutions for two wave numbers $k_0 = 2\pi/3\,\mathrm{m}^{-1}$ and $k_0 = 6\pi\,\mathrm{m}^{-1}$. (For interpretation of the colours in the figure(s), the reader is referred to the web version of this article.)

$$g(\varphi_x) = \frac{ik_0}{4\pi}\sum_{n=0}^{\infty}(2n+1)h_n(k_0 r_x)\left[j_n(k_0 r_y) - \alpha_n(k_0 R)h_n(k_0 r_y)\right]\times \left[\sum_{m=0}^{\infty}\epsilon_m\frac{(n-m)!}{(n+m)!}\cos(m\varphi_x)\,P_n^m(0)P_n^m(0)\right]. \tag{18}$$

The calculation differs from the previous paragraph 5.1.3 in the sense that for all $\boldsymbol{x}$ values, $G_T(\boldsymbol{x}, \mathbf{Z})$ must be determined for all $\mathbf{Z} \in \Gamma$ before determining $G_T(\boldsymbol{x}, \boldsymbol{y})$. Therefore the calculations are longer than in the previous paragraph.

In Fig. 3, the agreement reported between the numerical and analytical solutions is again very good. We obtain the same far field pattern as in 5.1.3. This cannot be explained by the reciprocity of the Green's function because between the two paragraphs, $\boldsymbol{x}$ and $\boldsymbol{y}$ are not simply exchanged, only the choice of the fixed parameter is changed. It is rather due to the fact that when r_x and r_y are fixed, the Green's function depends only on the angle $\widehat{(\boldsymbol{x}, \boldsymbol{y})} = \varphi_x - \varphi_y$ between $\boldsymbol{x}$ and $\boldsymbol{y}$, as seen in (16). This is why (18) is exactly (17) with φ_y replaced by φ_x.

Note that the evaluation in Fig. 3 has been performed only to test the numerical scheme. In practice we could use the reciprocity of the Green's function to speed up the calculations:

$$G_S(\boldsymbol{x}, \boldsymbol{y}) = G_S(\boldsymbol{y}, \boldsymbol{x}) = \int_{\Gamma} \partial_{\boldsymbol{n_Z}} G_0(\boldsymbol{x}, \mathbf{Z}) G_T(\boldsymbol{y}, \mathbf{Z}) dS_{\mathbf{Z}}.$$

Since $\boldsymbol{y}$ is fixed, as in 5.1.3 we recover the situation with only one costly step, which is to determine $G_T(\boldsymbol{y}, \mathbf{Z})$ for all $\mathbf{Z}$ on the surface. Then $\int_{\Gamma} \partial_{\boldsymbol{n_Z}} G_0(\boldsymbol{x}, \mathbf{Z}) G_T(\boldsymbol{y}, \mathbf{Z}) dS_{\mathbf{Z}}$ is easily evaluated for varying $\boldsymbol{x}$ by means of a matrix-vector product.

Note also that since the observation point $\boldsymbol{x}$ is far, a far-field approximation of G_T could be used, it is determined in Appendix B. We did not use this far-field approximation because we focus on the validation process in order to test precisely the accuracy of the numerical results.

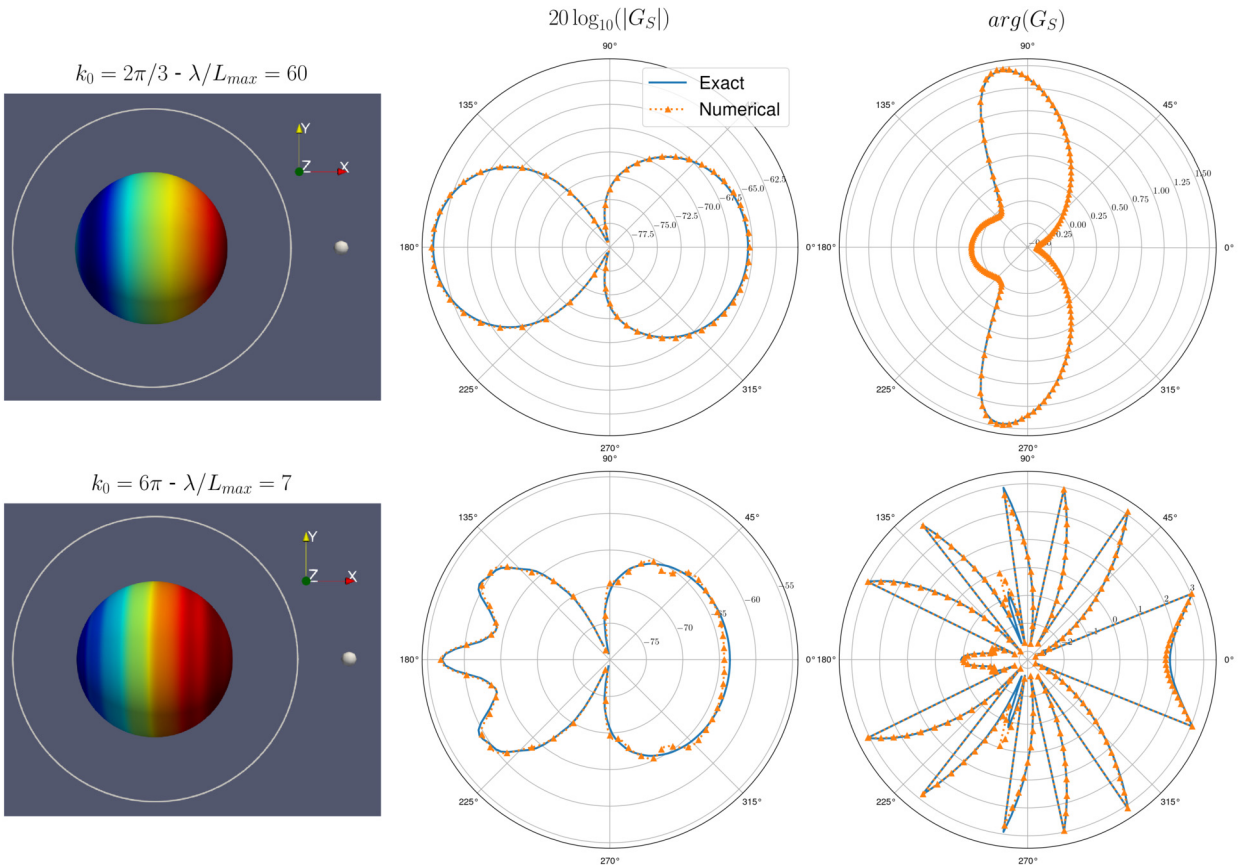

Fig. 2. Relative Green's function $G_S(\boldsymbol{x}, \boldsymbol{y})$ for a sphere for a fixed observation point at $\boldsymbol{x} = (100\,\mathrm{m}, 0, 0)$ and a varying source on the circle of radius $r_y = 1.1\,\mathrm{m}$ in the plane $y_3 = 0$. Comparison between the numerical function and the exact function for two wave numbers $k_0 = 2\pi/3\,\mathrm{m}^{-1}$ and $k_0 = 6\pi\,\mathrm{m}^{-1}$.

Eventually we test the method in Eq. (14) to evaluate derivatives of the Green's function. In Fig. 4 are represented the directivities of the second derivative $\partial^2 G_S/\partial y_1^2$. Once again the agreement between the numerical and analytical solutions is very good.

5.2. Validation for a cylinder

We consider an infinite cylinder of axis x_3 and of radius R. We introduce the cylindrical coordinates (r_x, θ_x, x_3) such that $x_1 = r_x \cos\theta_x$, $x_2 = r_x \sin\theta_x$ with $r_x^2 = x_1^2 + x_2^2$. In a same way we introduce $y_1 = r_y \cos\theta_y$, $y_2 = r_y \sin\theta_y$.

5.2.1. Analytical Green's function for a cylinder

Performing a Fourier transform along the x_3 axis, the Green's function is found of the form [21]

$$G_T(\boldsymbol{x}, \boldsymbol{y}) = \sum_{m=0}^{\infty} \epsilon_m G_m(\boldsymbol{x}, \boldsymbol{y}) \cos\left[m(\theta_x - \theta_y)\right], \tag{19}$$

with $\epsilon_0 = 1$, $\epsilon_m = 2$. For $r_x > r_y$, it is found

$$G_m(\boldsymbol{x}, \boldsymbol{y}) = \frac{i}{8\pi} \int_{\mathbb{R}} H_m(\gamma r_x) \left[J_m(\gamma r_y) - \alpha_m(\gamma R) H_m(\gamma r_y)\right] e^{iq(x_3 - y_3)} dq, \tag{20}$$

with $\gamma(q) = \sqrt{k_0^2 - q^2}$ and $\alpha_m(u) = J_m'(u)/H_m'(u)$.

This expression is exact and explicit but requires to perform numerically an inverse Fourier transform, which is not an easy task in particular because the integrand decreases slowly when $|q| \to \infty$. An approximate expression of the Green's function can be derived, easier to evaluate in practice. When considering the far field $r_x \gg r_y$, using the stationary phase theorem, the integral disappears (see proof in Appendix A) and it is found

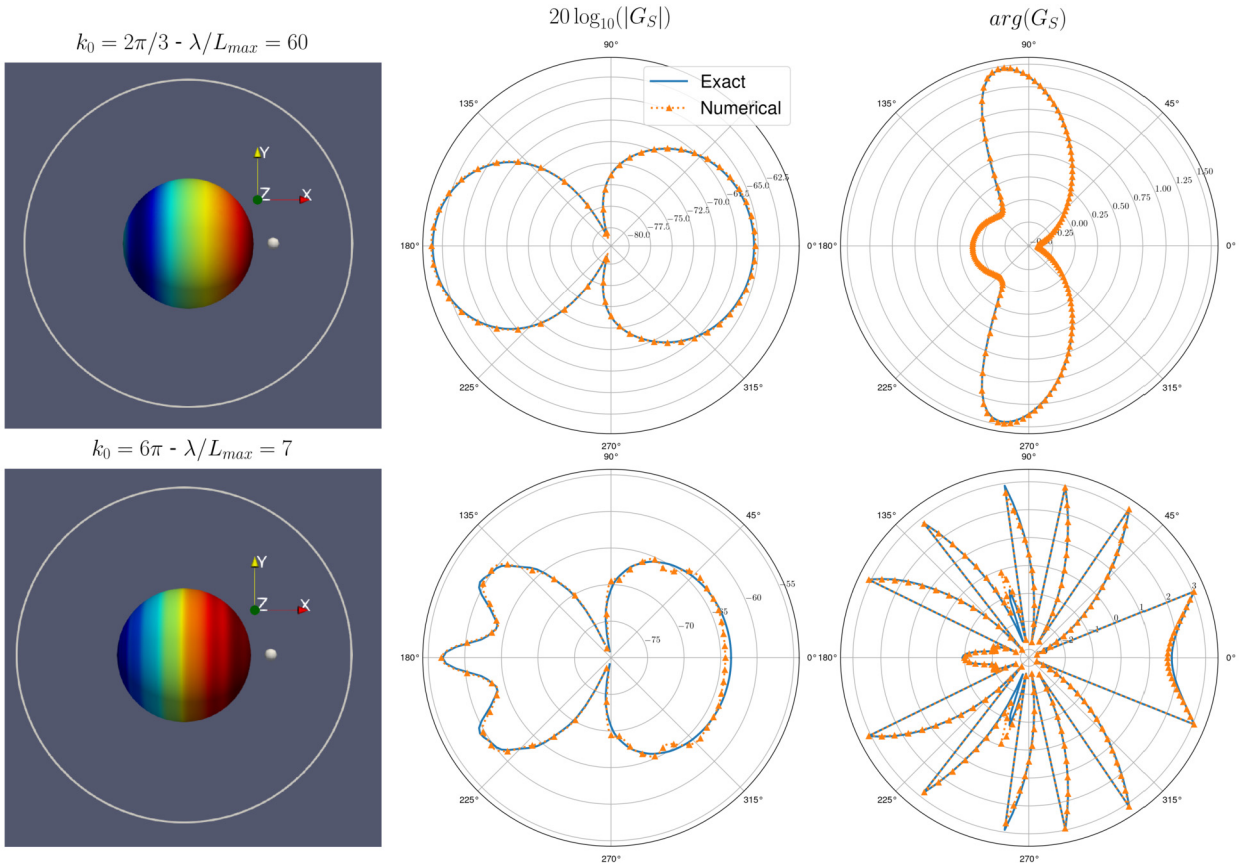

Fig. 3. Relative Green's function $G_S(\boldsymbol{x}, \boldsymbol{y})$ for a sphere for the fixed source at $\boldsymbol{y} = (1.1\,\mathrm{m}, 0, 0)$ and a varying observation point on the circle of radius $r_x = 100\,\mathrm{m}$ in the plane $x_3 = 0$. Comparison between the numerical and analytical solutions for two wave numbers $k_0 = 2\pi/3\,\mathrm{m}^{-1}$ and $k_0 = 6\pi\,\mathrm{m}^{-1}$.

$$G_m(\boldsymbol{x}, \boldsymbol{y}) \sim \frac{e^{ik_0|\boldsymbol{x}-y_3\boldsymbol{e}_3|}}{4\pi\,|\boldsymbol{x}-y_3\boldsymbol{e}_3|}\left[J_m\left(\frac{k_0 r_x r_y}{|\boldsymbol{x}-y_3\boldsymbol{e}_3|}\right) - \alpha_m\left(\frac{k_0 r_x R}{|\boldsymbol{x}-y_3\boldsymbol{e}_3|}\right) H_m\left(\frac{k_0 r_x r_y}{|\boldsymbol{x}-y_3\boldsymbol{e}_3|}\right)\right] e^{-i\pi m/2}, \tag{21}$$

with $|\boldsymbol{x}-y_3\boldsymbol{e}_3|^2 = x_1^2 + x_2^2 + (x_3-y_3)^2$. In particular, if the source and the observation points are in the same transverse plane $x_3 = 0 = y_3$, we get the extra simplification $|\boldsymbol{x}-y_3\boldsymbol{e}_3| = r_x$ and thus

$$G_m(\boldsymbol{x}, \boldsymbol{y}) = \frac{e^{ik_0 r_x}}{4\pi r_x}\left[J_m\left(k_0 r_y\right) - \alpha_m\left(k_0 R\right) H_m\left(k_0 r_y\right)\right] e^{-i\pi m/2}.$$

Note that an alternative and simpler expression of the Green's function exists, the compact Green's function [22]

$$G_{\text{compact}}(\boldsymbol{x}, \boldsymbol{y}) = \frac{e^{ik_0 r_x}}{4\pi r_x}\left[1 - \frac{ik_0}{r_x}(x_1 Y_1 + x_2 Y_2 + x_3 Y_3)\right],$$

with $Y_1 = y_1\left(1 + \dfrac{R^2}{y_1^2+y_2^2}\right)$, $Y_2 = y_2\left(1 + \dfrac{R^2}{y_1^2+y_2^2}\right)$ and $Y_3 = y_3$. Compared to the approximation we use, the compact Green's function is also valid only if $k_0 r_x \gg 1$ but also $k_0 R, k_0 r_y \ll 1$. In practice the validity domain is rather restricted, it is found to be valid only at low frequencies and for a source in the very close vicinity of the cylinder. For all these reasons, we cannot use it as a reference solution.

5.2.2. Comparison of analytical and numerical Green's functions

On the contrary to the analytical Green's function, the numerical evaluation for an infinite cylinder cannot be performed with the BEM, as this method requires a mesh and thus a bounded three-dimensional geometry. Therefore we consider a cylinder of radius $R = 1\,\mathrm{m}$ and of finite length $L = 20\,\mathrm{m}$. The FM-BEM is used with 125 852 DOFs with a largest mesh size of $L_{\max} = 50\,\mathrm{mm}$. As for the sphere, we have made three tests: we have compared the Green's functions (i) for a fixed observation point and a source on the cylinder surface or (ii) a source moving around the cylinder and (iii) for a fixed source and a moving observation point. In the three cases the agreement is good and we only show in Fig. 5 the results

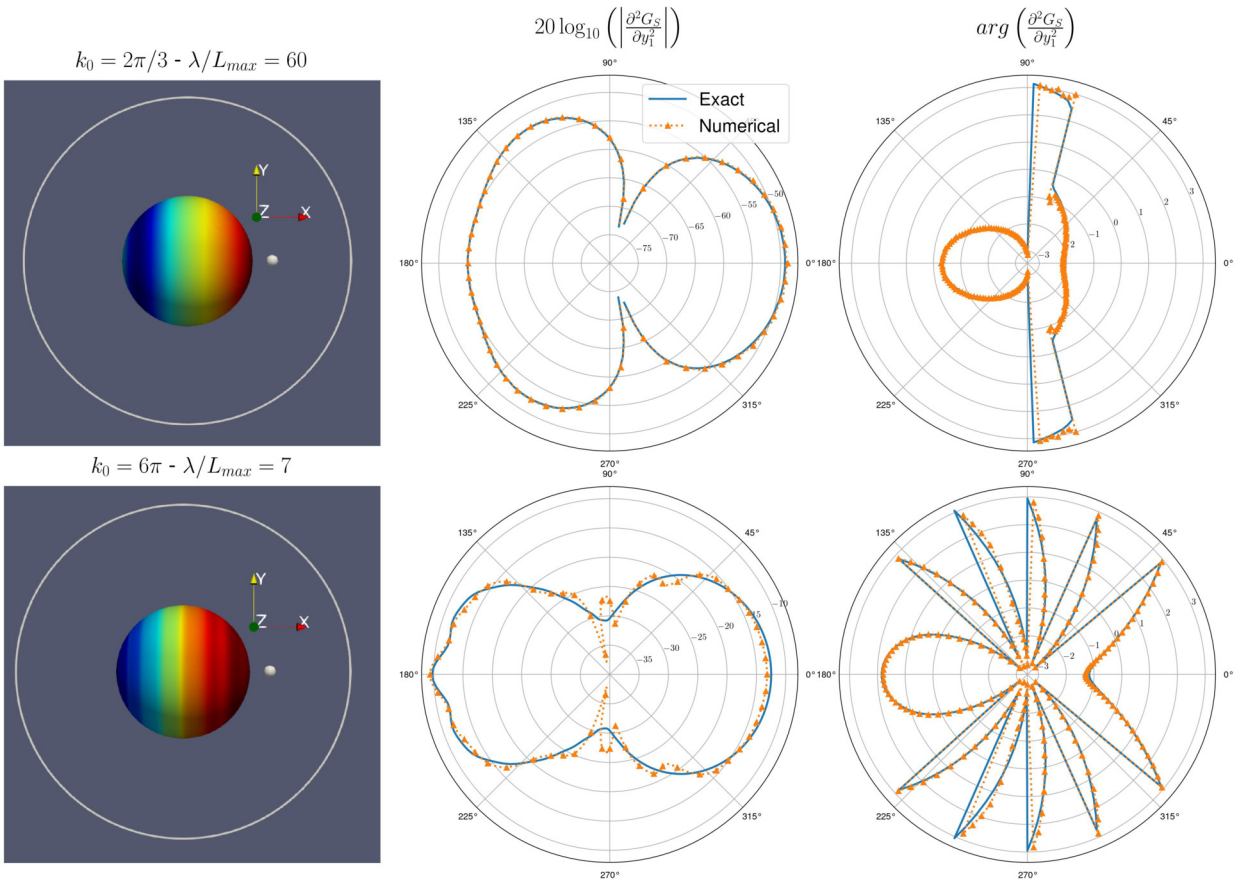

Fig. 4. Relative Green's function second derivative $\partial^2 G_S/\partial y_1^2$ for a sphere for the fixed source at $\boldsymbol{y} = (1.1\,\mathrm{m}, 0, 0)$ and a varying observation point on the circle of radius $r_x = 100\,\mathrm{m}$ in the plane $x_3 = 0$. Comparison between the numeric analytical solutions for two wave numbers $k_0 = 2\pi/3\,\mathrm{m}^{-1}$ and $k_0 = 6\pi\,\mathrm{m}^{-1}$.

for the case (ii): evaluation of $G_S(\boldsymbol{x}, \boldsymbol{y})$ for a fixed source at $\boldsymbol{y} = (1.1\,\mathrm{m}, 0, 0)$ and an observation point on the circle in the plane $x_3 = 0$, at $r_x = 100\,\mathrm{m}$, thus $\boldsymbol{x} = r_x(\cos\theta_x, \sin\theta_x, 0)$. Note that the agreement between numerical and theoretical results for a finite size mesh cannot be perfect, since (19) is valid for an infinite cylinder.

To test the derivatives of the Green's function, in Fig. 6 are represented the results for $\partial^2 G_S(\boldsymbol{x}, \boldsymbol{y})/\partial y_1^2$ and the agreement between numerical and theoretical results is very satisfactory.

5.3. Validation for a semi-infinite plane

The last validation case for which we have an explicit solution is a semi-infinite plane corresponding to $x_1 < 0$, $x_2 = 0$. As for the cylinder, we keep the cylindrical coordinates (r_x, θ_x, x_3) for the observation point and (r_y, θ_y, y_3) for the source.

5.3.1. Analytical Green's function for a semi-infinite plane

Performing a Fourier transform along the x_3 axis, the Green's function is found of the form [23]

$$G_T(\boldsymbol{x}, \boldsymbol{y}) = \sum_{m=0}^{\infty} \epsilon_m G_m(\boldsymbol{x}, \boldsymbol{y}) \cos\left(\frac{m}{2}(\theta_x + \pi)\right) \cos\left(\frac{m}{2}(\theta_y + \pi)\right),$$

with, for $r_x > r_y$:

$$G_m(\boldsymbol{x}, \boldsymbol{y}) = \frac{i}{8\pi} \int_{\mathbb{R}} H_{\frac{m}{2}}(\gamma r_x)\, J_{\frac{m}{2}}(\gamma r_y)\, e^{iq(x_3 - y_3)} dq,$$

where $\gamma(q) = \sqrt{k_0^2 - q^2}$.

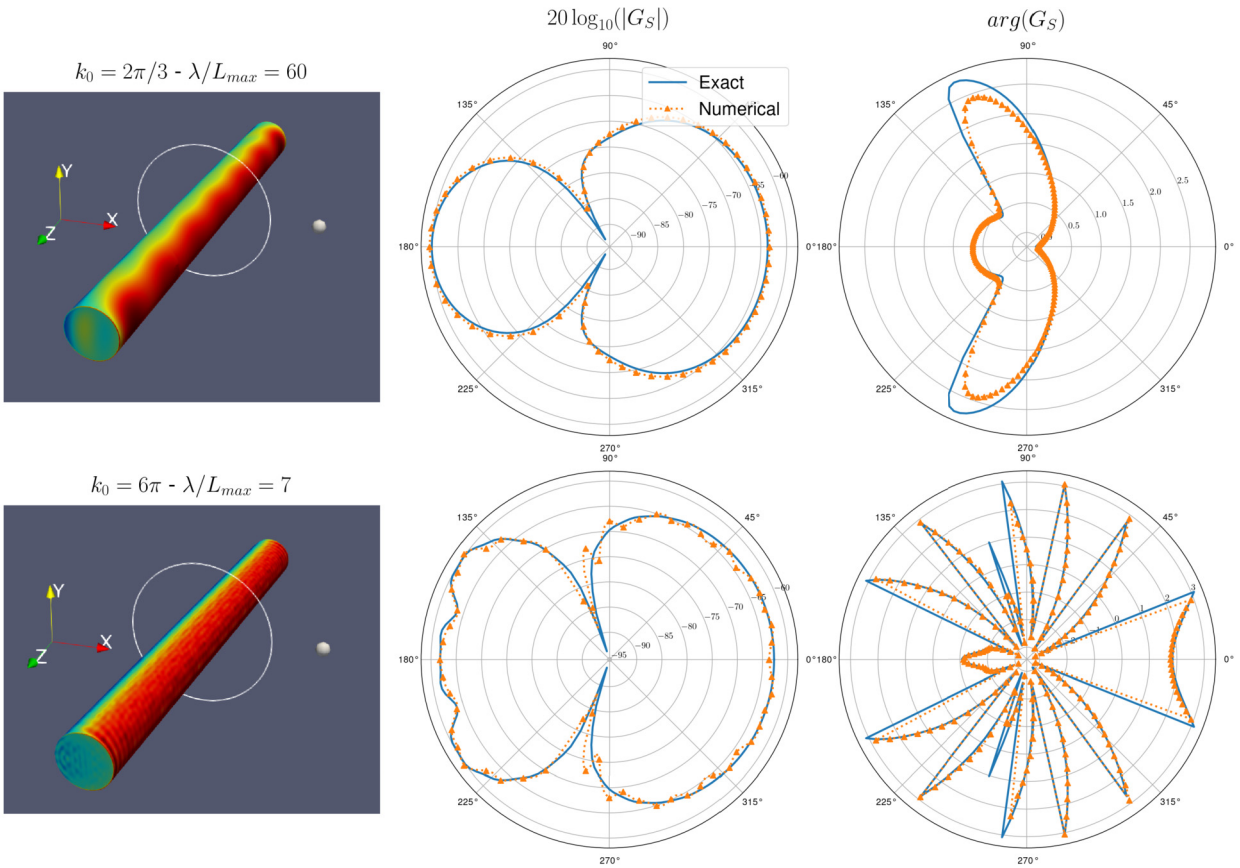

Fig. 5. Relative Green's function $G_S(\boldsymbol{x}, \boldsymbol{y})$ for a cylinder of radius $R = 1\,\text{m}$ for the fixed observation point at $\boldsymbol{x} = (100\,\text{m}, 0, 0)$ and a source varying on the circle of radius $r_y = 1.1\,\text{m}$ in the plane $y_3 = 0$. Comparison between the numerical and analytical solutions for two wave numbers $k_0 = 2\pi/3\,\text{m}^{-1}$ and $k_0 = 6\pi\ \text{m}^{-1}$.

As for the cylinder case, the stationary phase theorem leads to a simplified formula for the far field $r_x \gg r_y$ [23]:

$$G_m(\boldsymbol{x}, \boldsymbol{y}) = \frac{e^{ik_0|\boldsymbol{x}-y_3\boldsymbol{e}_3|}}{4\pi\,|\boldsymbol{x}-y_3\boldsymbol{e}_3|} J_{\frac{m}{2}}\left(\frac{k_0 r_x r_y}{|\boldsymbol{x}-y_3\boldsymbol{e}_3|}\right) e^{-i\pi m/4},$$

with $|\boldsymbol{x}-y_3\boldsymbol{e}_3|^2 = x_1^2 + x_2^2 + (x_3-y_3)^2$. In particular if $x_3 = 0 = y_3$, $|\boldsymbol{x}-y_3\boldsymbol{e}_3| = r_x$, leading to

$$G_m(\boldsymbol{x}, \boldsymbol{y}) = \frac{e^{ik_0 r_x}}{4\pi r_x} J_{\frac{m}{2}}(k_0 r_y) e^{-i\pi m/4}.$$

This approximation will be used as a reference solution in the numerical tests. Note that as for the cylinder case, a compact Green's function, less precised but easier to evaluate, can be derived using further simplifications. Indeed restricting the sum to $m \leq 1$ and considering $k_0 r_y \ll 1$ lead to

$$G_{\text{approx}}(\boldsymbol{x}, \boldsymbol{y}) = \frac{e^{ik_0 r_x}}{4\pi r_x}\left[1 + 2\sqrt{\frac{2k_0 r_y}{\pi}}\sin\left(\frac{\theta_x}{2}\right)\sin\left(\frac{\theta_y}{2}\right)e^{-i\pi/4}\right],$$

and we recover the compact half-plane Green's function [22]:

$$G_{\text{Howe}}(\boldsymbol{x}, \boldsymbol{y}) = \frac{e^{ik_0 r_x}}{4\pi r_x}\left[1 + 2\sqrt{\frac{2k_0}{\pi r_x}}\varphi^\star(\boldsymbol{x})\varphi^\star(\boldsymbol{y})e^{-i\pi/4}\right],$$

with

$$\varphi^\star(\boldsymbol{y}) = \sqrt{r_y}\sin\left(\frac{\theta_y}{2}\right), \tag{22}$$

the velocity potential of the flow around the half-plane edge.

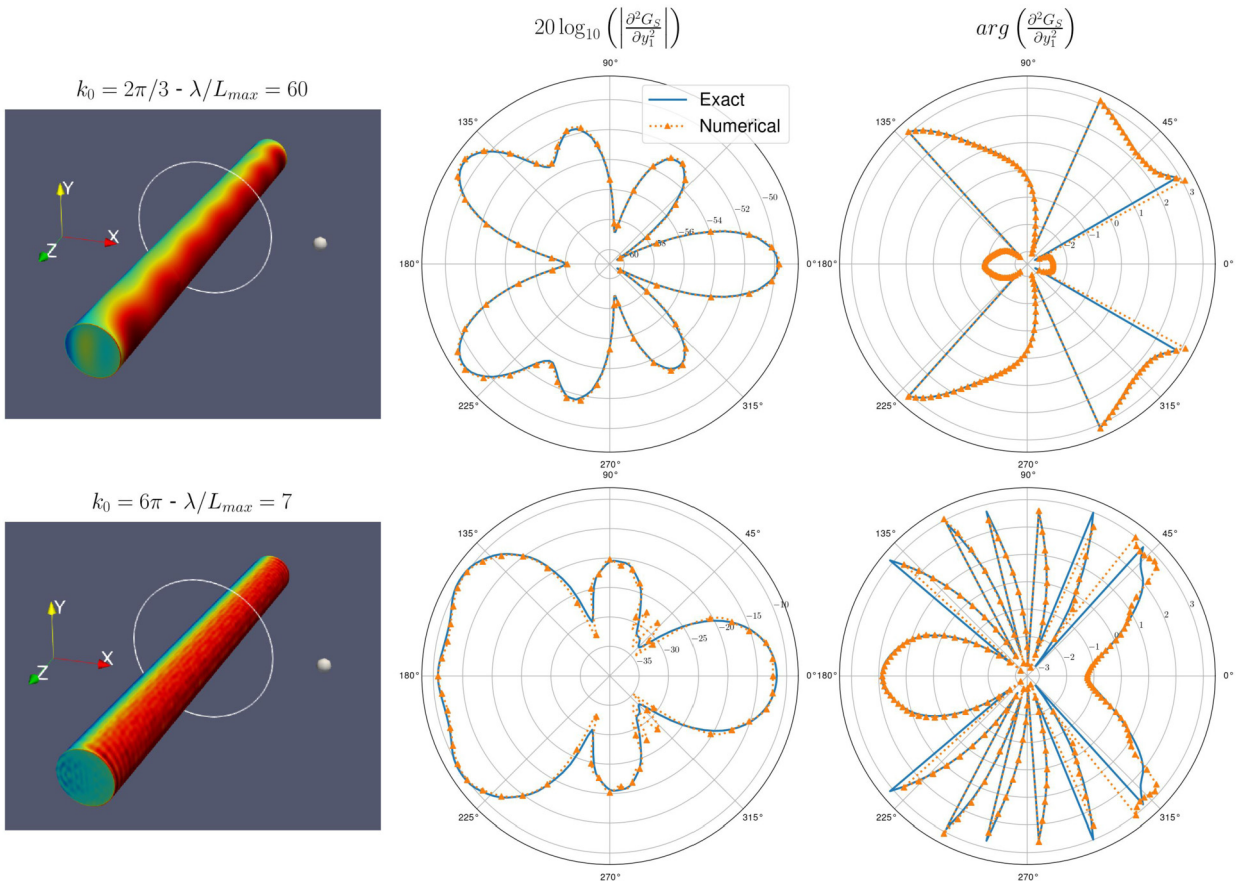

Fig. 6. Relative Green's function derivative $\partial^2 G_S/\partial y_1^2$ for a cylinder of radius $R = 1$ m for the fixed observation point at $\boldsymbol{x} = (100\,\text{m}, 0, 0)$ and a source varying on the circle of radius $r_y = 1.1$ m in the plane $y_3 = 0$. Comparison between the numerical and analytical solutions for two wave numbers $k_0 = 2\pi/3\,\text{m}^{-1}$ and $k_0 = 6\pi\ \text{m}^{-1}$.

5.3.2. Comparison of the analytical and numerical Green's functions

As for the cylinder case, the BEM requires to consider a three-dimensional volume. Therefore we consider a square finite plate of size $20\,\text{m} \times 20\,\text{m}$ with a small thickness of 1 cm. For this finite plate located at $]-20\,\text{m}, 0[\times]-0.5\,\text{cm}, 0.5\,\text{cm}[\times]-10\,\text{m}, 10\,\text{m}[$ to behave similarly to a semi-infinite plane, we focus on the near vicinity of the plate: we take a source at $\boldsymbol{y} = (-1.\,\text{m}, 0.1\,\text{m}, 0.)$, thus close to the plate and to the side $x_1 = 0$ of the plate, a small wavelength $\lambda_0 = 0.3\,\text{m}$ ($k_0 = 20\,\text{m}^{-1}$) and a close observation point at $r_x = 2\,\text{m}$. The FM-BEM method is used with 1 020 000 DOFs.

In Fig. 7 we compare the Green's functions for a fixed source and an observation point moving on the circle $r_x = 2\,\text{m}$ in the plane $x_3 = 0$, thus $\boldsymbol{x} = r_x(\cos\theta_x, \sin\theta_x, 0)$. The agreement is very satisfactory. As for the cylinder case, the differences between the two solutions are due to a finite size effect as numeric is done for a finite plate.

6. Efficiency of the method for complex geometries

Finally to illustrate the potential of the numerical method and to highlight its wide range of applications, we have considered less academic geometries: a NACA profile and a marine propeller. Contrary to the previous paragraph, no explicit solutions exist for comparison.

6.1. NACA 0012 *profile*

The profile has a span of $L = 10\,\text{m}$, a chord $c = 0.2\,\text{m}$ and a thickness $h = 0.12c$. Calculations have been performed with the FM-BEM on a mesh with 45 150 DOFs with a largest mesh size of $L_{\text{max}} = 6.7\,\text{mm}$. The source is located 1 cm above the leading edge, at $\boldsymbol{y} = (0., 0.01\,\text{m}, 0.)$. The observation point moves on a circle of radius $r_x = 2\,\text{m}$. Comparison is done with the only available explicit formula, the Multiple Scattering Green function [24], derived for a finite plate of no thickness, not for an airfoil of varying finite thickness:

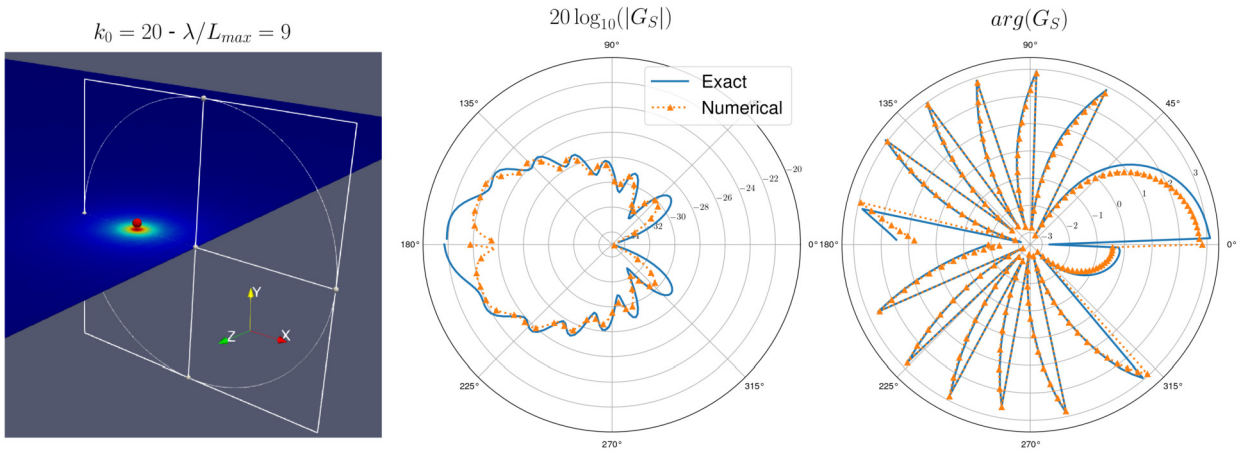

Fig. 7. Relative Green's function $G_S(\boldsymbol{x}, \boldsymbol{y})$ for a semi-infinite plate for the fixed source at $\boldsymbol{y} = (-1.0\,\mathrm{m}, 0.1\,\mathrm{m}, 0.0)$ and a varying observation point on the circle of radius $r_x = 2\,\mathrm{m}$ in the plane $x_3 = 0$. Comparison between the numerical and analytical solutions for the wave number $k_0 = 20\,\mathrm{m}^{-1}$.

$$
\begin{cases}
G_{\mathrm{MS}}(\mathbf{x},\mathbf{y},\omega) &= G_1(\mathbf{x},\mathbf{y},\omega) + G_{\mathrm{LE}}(\mathbf{x},\mathbf{y},\omega) + G_{\mathrm{TE}}(\mathbf{x},\mathbf{y},\omega), \\
G_1(\mathbf{x},\mathbf{y},\omega) &= \dfrac{-e^{ik_0|\mathbf{x}-y_3\mathbf{i_3}|}}{4\pi|\mathbf{x}-y_3\mathbf{i_3}|} - \dfrac{\sqrt{k_0 r_x}\sin(\theta_x/2)\sqrt{r_y}\sin(\theta_y/2)}{\pi\sqrt{2i\pi}|\mathbf{x}-y_3\mathbf{i_3}|^{3/2}} e^{ik_0|\mathbf{x}-y_3\mathbf{i_3}|}, \\
G_{\mathrm{LE}} &= \dfrac{\sqrt{k_0\sin\psi_x}\varphi^*(\mathbf{y})e^{ik_0(|\mathbf{x}'|+c\sin\psi_x)}}{i\pi^{3/2}|\mathbf{x}|(1+e^{2ik_0c\sin\psi_x}/2\pi ik_0c\sin\psi_x)} \mathcal{F}\left(2\sqrt{\dfrac{k_0c\sin\psi_x\cos^2(\theta_x/2)}{\pi}}\right), \\
G_{\mathrm{TE}} &= \dfrac{-\varphi^*(\mathbf{y})e^{ik_0(|\mathbf{x}|+2c\sin\psi_x)}}{\pi^2\sqrt{2ic}|\mathbf{x}|(1+e^{2ik_0c\sin\psi_x}/2\pi ik_0c\sin\psi_x)} \mathcal{F}\left(2\sqrt{\dfrac{k_0c\sin\psi_x\sin^2(\theta_x/2)}{\pi}}\right), \\
\mathcal{F}(x) &= \dfrac{1}{2+4.142x+3.492x^2+6.670x^3} + i\dfrac{1+0.926x}{2+1.792x+3.104x^2}.
\end{cases}
\tag{23}
$$

G_{LE} and G_{TE} are the leading edge and trailing edge contributions. φ^* is the potential flow defined in (22). Note that this Multiple Scattering Green's function is valid under rather drastic conditions: $L = \infty$, $h \ll r_y \ll c$, $k_0 r_y \ll 1$ and $k_0 c \gg 1$. The numerical tests cannot be done in the same conditions and that is why the comparison will not be perfect. Since we took $h = 0.12c$, the condition $h \ll c$ is correctly satisfied but none of the others since $h \sim r_y$, $L = 10\,\mathrm{m}$ and for $k_0 = 10\,\mathrm{m}^{-1}$, we get $k_0 c = 2$ which is not large.

For a fixed source and an observation point moving on the circle $\boldsymbol{x} = r_x(\cos\theta_x, \sin\theta_x, 0)$ with $r_x = 2\,\mathrm{m}$, the modulus and argument of the numerical Green's function are plotted versus θ_x, for $k_0 = 10\,\mathrm{m}^{-1}$ in Fig. 8 and $k_0 = 50\,\mathrm{m}^{-1}$ in Fig. 9. The agreement with the analytical Green function is not perfect, but we recall that this formula is far for being exact. The curvature of the NACA profile is found to have a strong influence on the directivity, as seen very clearly on the argument of the numerical Green's functions. Howe's formula built for a flat plate predicts an argument symmetric when $\theta_x \to -\theta_x$ whereas the numerical Green's argument is found strongly asymmetric. Of course if the source is placed in a symmetrical way, at $\boldsymbol{y} = (0.01\,\mathrm{m}, 0, 0)$ as in Fig. 10, the directivities are found symmetric as expected. Note that in this case Howe's formula with $\theta_y = 0$ predicts 0 and thus the results are not reported.

7. Marine propeller

To finish we consider a complex geometry whose mesh is shown in Fig. 11, for which no approximate formula is available. The largest mesh size is $L_{\max} = 8\,\mathrm{mm}$ leading to 106 074 DOFs. In Fig. 12 is represented the second derivative of the Green's function $(\partial^2 G_S/\partial y_1^2)(\boldsymbol{x}, \boldsymbol{y})$ versus the position $\boldsymbol{y}$ of the source for two wave numbers $k_0 = 10\,\mathrm{m}^{-1}$ (left) and $k_0 = 100\,\mathrm{m}^{-1}$ (right). The observation point is fixed on the axis of the propeller at 100 m and the propeller radius is 0.5 m.

For this complex geometry, since we cannot compare the numerical results to some exact results, we have chosen to test different acceleration methods. We compare in Fig. 13 the performances of the standard and fast BEMs. We report for various wave numbers (from 1 to $130\,\mathrm{m}^{-1}$) the number of iterations, the memory requirements, the total computational time and the computational time for one iteration. For each wave number k_0 given in m^{-1} we also indicate the associated numbers of discretization points per wavelengths $\lambda/L_{\max}$ with $L_{\max} = 8\,\mathrm{mm}$ the largest mesh size.

As expected, the number of iterations to solve the BEM problem (subplot a) increases with the frequency of the problem and since no preconditioner is used in this example, for large wave numbers, the number of iterations becomes large. Moving to the memory requirements (subplot b), we observe the expected constant footprint for the standard BEM. Since the number of DOFs is fixed, the cost does not change from one frequency to another. Importantly, fast BEMs drastically

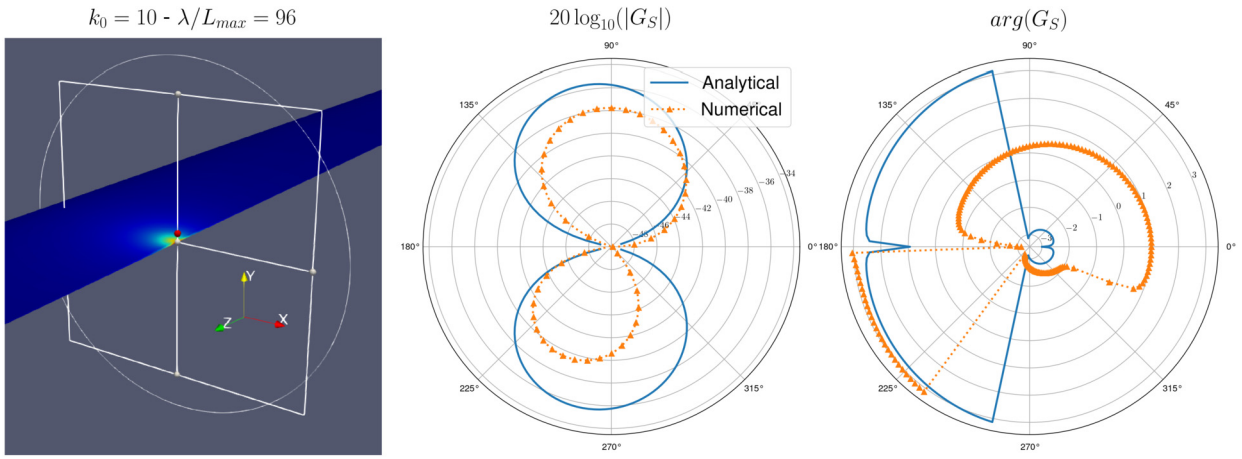

Fig. 8. Relative Green's function $G_S(\boldsymbol{x}, \boldsymbol{y})$ for a NACA profile for the fixed source at $\boldsymbol{y} = (0., 0.01\,\mathrm{m}, 0.)$ and a varying observation point on the circle of radius $r_x = 2\,\mathrm{m}$ in the plane $x_3 = 0$. Comparison between the numerical and analytical solutions for the wave number $k_0 = 10\,\mathrm{m}^{-1}$.

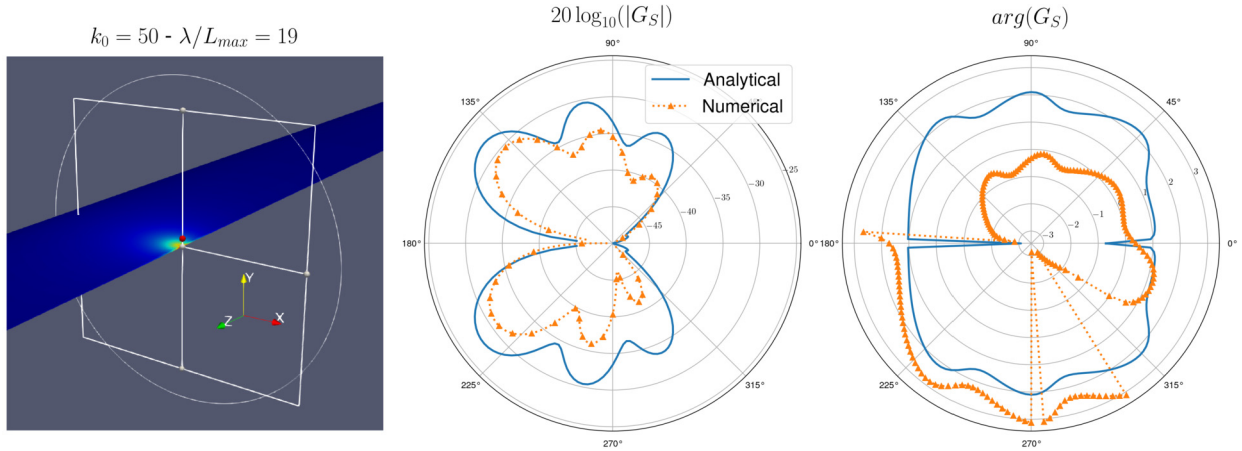

Fig. 9. Relative Green's function $G_S(\boldsymbol{x}, \boldsymbol{y})$ for a NACA profile for the fixed source at $\boldsymbol{y} = (0, 0.01\,\mathrm{m}, 0.)$ and a varying observation point on the circle of radius $r_x = 2\,\mathrm{m}$ in the plane $x_3 = 0$. Comparison between the numerical and analytical solutions for the wave number $k_0 = 50\,\mathrm{m}^{-1}$.

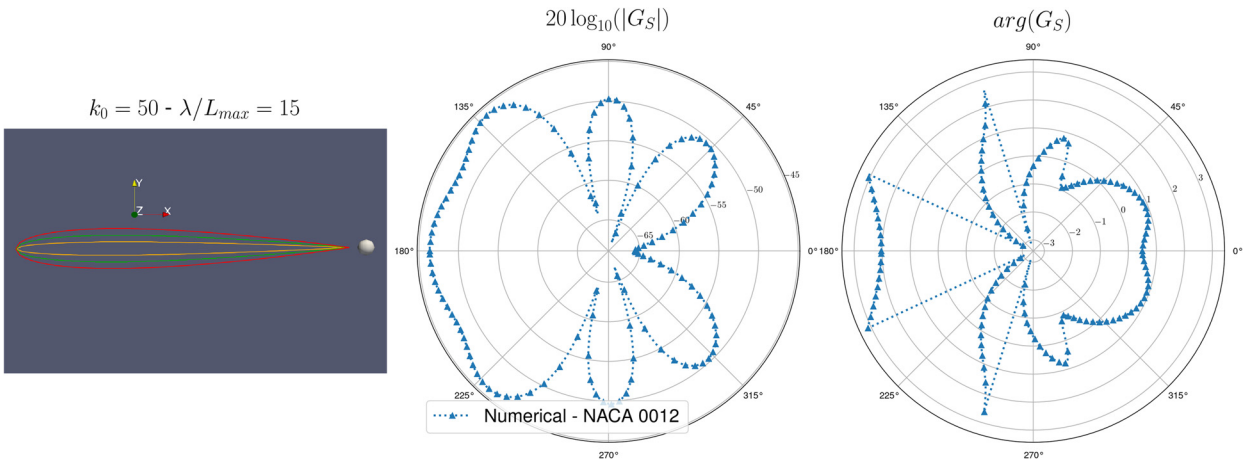

Fig. 10. Relative Green's function $G_S(\boldsymbol{x}, \boldsymbol{y})$ for a NACA profile for the fixed source at $\boldsymbol{y} = (0.01\,\mathrm{m}, 0.0, 0.0)$, a varying observation point on the circle of radius $r_x = 2\,\mathrm{m}$ in the plane $x_3 = 0$ and for the wave number $k_0 = 50\,\mathrm{m}^{-1}$. Only the numerical solutions are plotted since the numerical solution is equal to 0 for this source position.

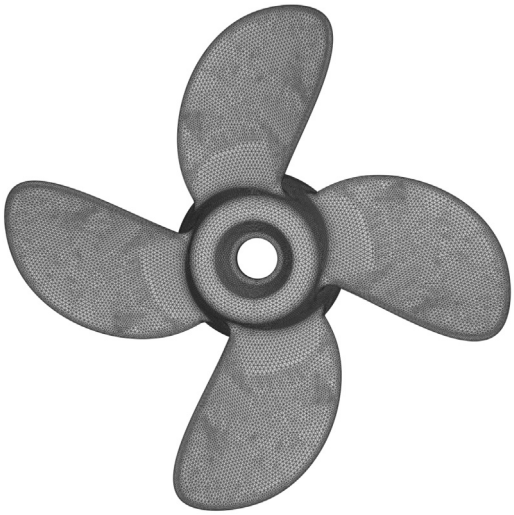

Fig. 11. Mesh of a marine propeller.

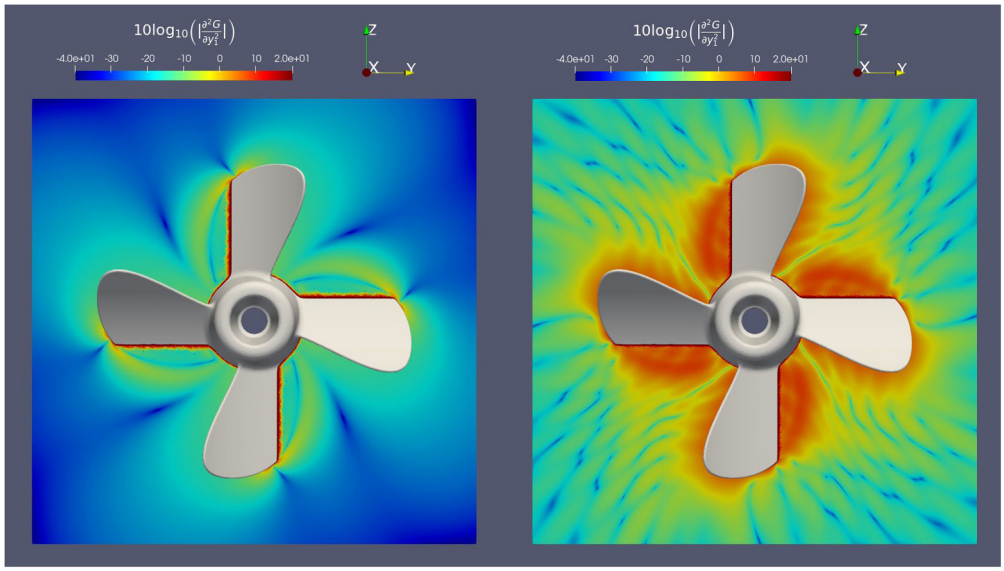

Fig. 12. Relative Green's function second derivative $\partial^2 G_S/\partial y_1^2(\boldsymbol{x}, \boldsymbol{y})$ for an observation point at $\boldsymbol{x} = (100\,\mathrm{m}, 0.0, 0.0)$ and a varying source point in the plane (y_2, y_3), for two wave numbers $k_0 = 10\,\mathrm{m}^{-1}$ (left) and $k_0 = 100\,\mathrm{m}^{-1}$ (right). The propeller radius is 0.5 m. Mesh with 106074 DOFs.

reduce the memory requirements compared to standard BEMs. For $\mathcal{H}$-BEM, since the maximum rank along the admissible blocks is known to increase linearly with the frequency [18], we observe a linear complexity. On the other hand, for a low frequency, the mesh is over-refined, leading to a suboptimal use of the FM-BEM. In particular, the only part of the system matrix stored in FM-BEMs is the one related to near contributions. Since the size of the near contributions is related to the frequency of the problems, for low wave numbers the near contributions include a lot of discretization points. This explains the fact that memory requirements decrease, for a fixed discretization, with respect to the frequency with the expected optimal behaviour around the usual parameter of ten points per wavelength. Concerning the optimal memory requirements, the numerical results are in agreement with the theory. Subplot c represents the total computational time costs for the three methods. The standard BEM is seen to be prohibitively expensive with a computational cost increasing due to the increase of the number of iterations. Fast BEMs are again seen to be very efficient with a drastic reduction of the computational cost even when the FM-BEM is not used in its optimal frequency range. Since these computational times also include the number of iterations, subplot d presents only the most expensive part of the BEM solution: the evaluation of a matrix-vector product. As expected, this cost is constant for standard BEM since the number of DOFs is fixed. The cost for $\mathcal{H}$-BEM increases linearly due to the increase of the maximum rank (already observed in the memory requirements). The cost for the FM-BEM is decreasing with the frequency similarly to memory requirements. For low wave numbers again, the cost to perform the matrix-vector product for near contributions is taking more time due to the use of an over-refined mesh.

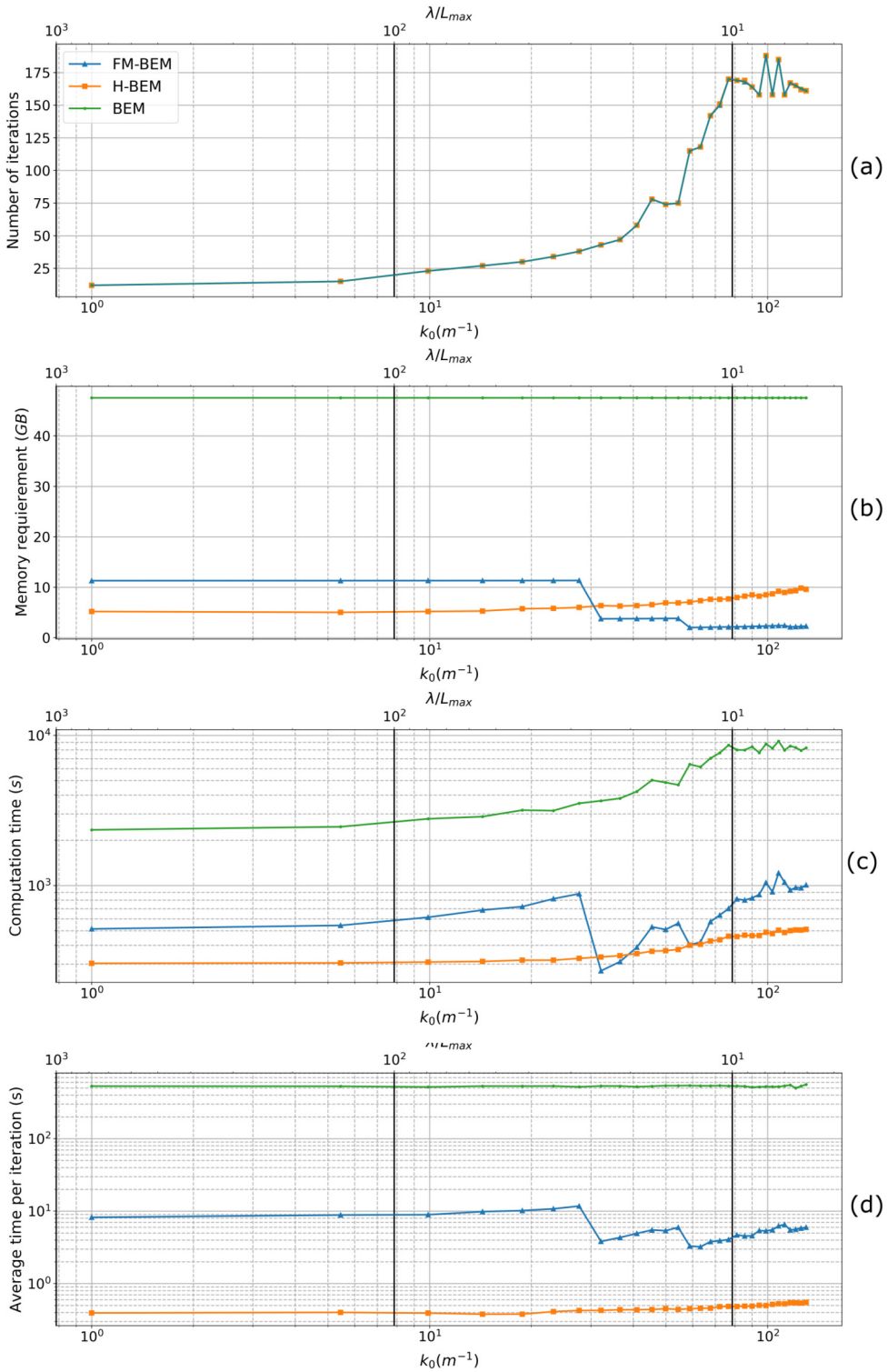

Fig. 13. Comparison of the standard, FM-BEM and $\mathcal{H}$-BEMs for the complex geometry represented in Fig. 11. From top to bottom: number of iterations, memory requirements, total computational time and computational time for one iteration.

Importantly, the cost to perform one matrix-vector product with the $\mathcal{H}$-BEM is seen to be well below the cost with the FM-BEM. Most of the time in $\mathcal{H}$-BEM is spent in the evaluation of the $\mathcal{H}$-matrix representation of the system but then the matrix-vector product is very fast. These results advocate in favour of the use of $\mathcal{H}$-BEM. FM-BEM are in theory the most efficient approach for wave propagation problems with the optimal complexity. But this is true for academic problems with an optimal uniform mesh refinement of approximately ten points per wavelength and when a small number of iterations is required to achieve convergence. In industrial applications, these requirements are not always possible to fulfil. Even though $\mathcal{H}$-BEM are not optimal, they permit with a simple implementation to obtain a very fast BEM robust in an industrial context.

8. Conclusions and future work

We have developed an efficient numerical method to determine tailored three-dimensional Helmholtz Green's functions in presence of an obstacle of arbitrary shape with a Neumann boundary condition. This function is important to determine the flow noise, like the hydrodynamic noise radiated by a ship for instance, obtained by solving Lighthill's wave equation. Tailored Green's functions are known analytically for canonical geometries. In this work, we have presented a method to compute them numerically and efficiently for arbitrary shapes. First an integral equation is derived, expressing the rigid Green's function versus the free space Green's function Then a boundary element method is used to compute numerical Green's functions or their derivatives which are important to compute the aero or hydroacoustic components. In order to reduce computational cost, the boundary element method is accelerated by two methods: a fast multipole method and/or hierarchical matrices. The numerical methods have been tested on simple geometries for which exact functions can be determined (sphere, cylinder, half plane) and for realistic geometries, rigid Green's functions have been computed and associated directivity diagrams have been determined.

Concerning possible extensions, in this work only the case of a rigid boundary has been considered. In the future, we plan to extend to more general boundary conditions, notably a Robin condition to consider impedant boundary conditions, possibly absorbing for complex impedances.

CRediT authorship contribution statement

- Stéphanie Chaillat took in charge the Methodology, Software and Resources,
- Benjamin Cotté took in charge the Conceptualization and Supervision,
- Jean-François Mercier took in charge the Methodology, Formal analysis, Writing - Original Draft and Preparation Review & Editing,
- Gilles Serre took in charge the Conceptualization, Supervision, Project administration and Funding acquisition,
- Nicolas Trafny took in charge the Software Validation, Investigation, Data Curation and Visualization.

Declaration of competing interest

The authors declare that they have no known competing financial interests or personal relationships that could have appeared to influence the work reported in this paper.

Acknowledgements

The authors would like to thank Naval Group and Association Nationale Recherche et Technologie (ANRT) for supporting this work.

Appendix A. Far field cylinder Green's function

We wish to show that the m^{th} component $G_m(\boldsymbol{x}, \boldsymbol{y})$ given by (20) of the Green function defined in (19), simplifies in (21) when $r_x \gg r_y$. This is achieved following the approach developed in [23] for the case of a semi-infinite plate, based on the use of the stationary phase theorem [25]. The first step is to use the asymptotics for $\gamma r_x \gg 1$:

$$H_m(\gamma r_x) \sim \sqrt{\frac{2}{\pi \gamma r_x}} e^{i\gamma r_x} e^{-i\pi/4} e^{-i\pi m/2}.$$

From (20) it leads to the expression

$$G_m(\boldsymbol{x}, \boldsymbol{y}) \sim \frac{i}{8\pi} e^{-i\pi/4} e^{-i\pi m/2} f(\boldsymbol{x}, \boldsymbol{y}),$$

with

$$f(\boldsymbol{x}, \boldsymbol{y}) = \int_{\mathbb{R}} \sqrt{\frac{2}{\pi \gamma r_x}} \left[J_m(\gamma r_y) - \alpha_m(\gamma R) H_m(\gamma r_y) \right] e^{i\gamma r_x} e^{iq(x_3 - y_3)} dq.$$

To apply the stationary phase theorem, f is conveniently written

$$f(\boldsymbol{x},\boldsymbol{y}) = \int_{\mathbb{R}} g(q;\boldsymbol{x},\boldsymbol{y}) e^{i\varphi(q;\boldsymbol{x},\boldsymbol{y})} dq,$$

with

$$g(q;\boldsymbol{x},\boldsymbol{y}) = \sqrt{\frac{2}{\pi\gamma r_x}} \left\{ J_m\left[\gamma(q) r_y\right] - \alpha_m\left[\gamma(q)R\right] H_m\left[\gamma(q) r_y\right] \right\},$$

and with the phase $\varphi(q;\boldsymbol{x},\boldsymbol{y}) = \gamma(q) r_x + q(x_3 - y_3)$. The phase is stationary for $q = q_0 \equiv k(x_3 - y_3)/|\boldsymbol{x} - y_3\boldsymbol{e}_3|$ with $|\boldsymbol{x} - y_3\boldsymbol{e}_3|^2 = x_1^2 + x_2^2 + (x_3 - y_3)^2$. Then we have $\varphi(q_0) = k|\boldsymbol{x} - y_3\boldsymbol{e}_3|$ and $\varphi''(q_0) = -|\boldsymbol{x} - y_3\boldsymbol{e}_3|^3/(kr_x^2)$ (with of course $\varphi'(q_0) = 0$). Since $\varphi''(q_0) \neq 0$, the stationary phase theorem indicates that when $r_x \to \infty$,

$$f(\boldsymbol{x},\boldsymbol{y}) \sim g(q_0;\boldsymbol{x},\boldsymbol{y}) e^{i\varphi(q_0;\boldsymbol{x},\boldsymbol{y})} \sqrt{\frac{-2\pi}{i\varphi''(q_0)}}.$$

Using $\gamma(q_0) = kr_x/|\boldsymbol{x} - y_3\boldsymbol{e}_3|$, it leads to

$$G_m(\boldsymbol{x},\boldsymbol{y}) \sim \frac{e^{ik|\boldsymbol{x} - y_3\boldsymbol{e}_3|}}{4\pi|\boldsymbol{x} - y_3\boldsymbol{e}_3|} \times \left[J_m\left(\frac{kr_x r_y}{|\boldsymbol{x} - y_3\boldsymbol{e}_3|}\right) - \alpha_m\left(\frac{kr_x R}{|\boldsymbol{x} - y_3\boldsymbol{e}_3|}\right) H_m\left(\frac{kr_x r_y}{|\boldsymbol{x} - y_3\boldsymbol{e}_3|}\right) \right] e^{-i\pi m/2}.$$

Appendix B. Far-field approximation

Another interest of our approach is to easily give access to the far field radiation pattern of any obstacle. Indeed (7) can be simplified when the observation point is far. Using the Green's function reciprocity

$$G_T(\boldsymbol{x},\boldsymbol{y}) = G_T(\boldsymbol{y},\boldsymbol{x}) = G_0(\boldsymbol{y},\boldsymbol{x}) + \int_\Gamma \partial_{\boldsymbol{n}_\mathbf{Z}} G_0(\boldsymbol{x},\mathbf{Z}) G_T(\boldsymbol{y},\mathbf{Z}) dS_\mathbf{Z},$$

combined with (8) with $\boldsymbol{y}$ replaced by $\boldsymbol{x}$

$$\partial_{\boldsymbol{n}_\mathbf{Z}} G_0(\boldsymbol{x},\mathbf{Z}) = (\mathbf{Z} - \boldsymbol{x}) \cdot \boldsymbol{n}(\mathbf{Z}) \frac{ik|\mathbf{Z} - \boldsymbol{x}| - 1}{|\mathbf{Z} - \boldsymbol{x}|^3} \frac{e^{ik|\mathbf{Z} - \boldsymbol{x}|}}{4\pi},$$

it can be deduced that (7) can be written

$$G_T(\boldsymbol{x},\boldsymbol{y}) = \frac{e^{ik|\boldsymbol{y} - \boldsymbol{x}|}}{4\pi|\boldsymbol{y} - \boldsymbol{x}|} + \int_\Gamma (\mathbf{Z} - \boldsymbol{x}) \cdot \boldsymbol{n}(\mathbf{Z}) \frac{ik|\mathbf{Z} - \boldsymbol{x}| - 1}{|\mathbf{Z} - \boldsymbol{x}|^3} \frac{e^{ik|\mathbf{Z} - \boldsymbol{x}|}}{4\pi} G_T(\boldsymbol{y},\mathbf{Z}) dS_\mathbf{Z}. \tag{B.1}$$

This expression simplifies in the far field. When $|\boldsymbol{x}| \to \infty$, (B.1) simplifies in

$$G_T(\boldsymbol{x},\boldsymbol{y}) = \frac{e^{ik|\boldsymbol{x}|}}{4\pi|\boldsymbol{x}|} \left[1 + \left(-ik\frac{\boldsymbol{x}}{|\boldsymbol{x}|}\right) \cdot \int_\Gamma \boldsymbol{n}(\mathbf{Z}) e^{-ik\frac{\boldsymbol{x}}{|\boldsymbol{x}|}\cdot\mathbf{Z}} G_T(\boldsymbol{y},\mathbf{Z}) dS_\mathbf{Z} \right].$$

Introducing the unit direction vector $\boldsymbol{\xi} = \boldsymbol{x}/|\boldsymbol{x}|$ and defining the Fourier transform of any function $f(\mathbf{Z})$ by $\hat{f}(\boldsymbol{\xi}) = F[f](\boldsymbol{\xi}) = \int_\Gamma e^{-ik\boldsymbol{\xi}\cdot\mathbf{Z}} f(\mathbf{Z}) dS_\mathbf{Z}$, the simplified expression becomes

$$G_T(\boldsymbol{x},\boldsymbol{y}) = \frac{e^{ik|\boldsymbol{x}|}}{4\pi|\boldsymbol{x}|} \left[1 - ik\boldsymbol{\xi} \cdot \hat{\boldsymbol{F}}(\boldsymbol{y},\boldsymbol{\xi}) \right] \tag{B.2}$$

where we have noted $\hat{\boldsymbol{F}}(\boldsymbol{y},\boldsymbol{\xi}) = F[\boldsymbol{n}(\cdot) G_T(\boldsymbol{y},\cdot)](\boldsymbol{\xi})$. The advantage is that (B.2) does not depend on the position $\boldsymbol{x}$ but just on the direction $\boldsymbol{\xi} = \boldsymbol{x}/|\boldsymbol{x}|$. This is in particular useful to plot directivities.

Appendix C. Evaluation of the third derivatives of the free field Green function

In order to compute (14), the knowledge of the third derivatives of the free field Green's function is necessary. Let us recall that the free field Green's function is defined by

$$G_0(\boldsymbol{y},\mathbf{Z}) = \frac{e^{ik_0|\boldsymbol{y}-\mathbf{Z}|}}{4\pi\,|\boldsymbol{y}-\mathbf{Z}|}. \tag{C.1}$$

The normal derivative is

$$\partial_{\boldsymbol{n_Z}} G_0(\boldsymbol{y},\mathbf{Z}) = (\mathbf{Z}-\boldsymbol{y})\cdot\boldsymbol{n}(\mathbf{Z})\frac{ik_0|\mathbf{Z}-\boldsymbol{y}|-1}{|\mathbf{Z}-\boldsymbol{y}|^3}\frac{e^{ik_0|\mathbf{Z}-\boldsymbol{y}|}}{4\pi}. \tag{C.2}$$

If we define $\mathbf{r}=\boldsymbol{y}-\mathbf{Z}$ and $r=|\mathbf{r}|$ then:

$$\begin{cases} \dfrac{\partial r}{\partial y_i}=\dfrac{r_i}{r}, \quad \dfrac{\partial r}{\partial Z_i}=-\dfrac{r_i}{r} \\ \dfrac{\partial r^2}{\partial y_i}=2r_i, \quad \dfrac{\partial r^2}{\partial Z_i}=-2r_i \\ \dfrac{\partial r^3}{\partial y_i}=3rr_i, \quad \dfrac{\partial r^3}{\partial Z_i}=-3rr_i \\ \dfrac{\partial}{\partial y_i}(\mathbf{r}\cdot\mathbf{n})=n_i, \quad \dfrac{\partial}{\partial Z_i}(\mathbf{r}\cdot\mathbf{n})=-n_i \\ \dfrac{\partial r_i}{\partial y_j}=\delta_{ij}, \quad \dfrac{\partial r_i}{\partial Z_j}=-\delta_{ij}. \end{cases} \tag{C.3}$$

By introducing

$$f(r)=\frac{1-ik_0r}{r^3}e^{ik_0r}$$

the derivative of (C.2) with respect to y_i yields

$$\partial_{\boldsymbol{n_Z}}\frac{\partial G_0}{\partial y_i}(\boldsymbol{y},\mathbf{Z}) = \frac{1}{4\pi}\left[\frac{\partial f}{\partial y_i}(\mathbf{r}\cdot\mathbf{n})+f\frac{\partial}{\partial y_i}(\mathbf{r}\cdot\mathbf{n})\right], \tag{C.4}$$

where

$$\frac{\partial f}{\partial y_i}=\frac{r_i}{r^5}(k_0^2r^2+3ik_0r-3)\,e^{ik_0r}, \tag{C.5}$$

and

$$\frac{\partial}{\partial y_i}\left(e^{ik_0r}\right)=\frac{ik_0r_i}{r}e^{ik_0r} \tag{C.6}$$

Finally

$$\partial_{\boldsymbol{n_Z}}\frac{\partial^2 G_0}{\partial y_i\partial y_j}(\boldsymbol{y},\mathbf{Z}) = \frac{1}{4\pi}\left[\frac{\partial^2 f}{\partial y_i\partial y_j}(\mathbf{r}\cdot\mathbf{n})+\frac{\partial f}{\partial y_i}\frac{\partial}{\partial y_j}(\mathbf{r}\cdot\mathbf{n})++\frac{\partial f}{\partial y_j}\frac{\partial}{\partial y_i}(\mathbf{r}\cdot\mathbf{n})\right], \tag{C.7}$$

where

$$\begin{aligned}\frac{\partial^2 f}{\partial y_i\partial y_j} &= \frac{\partial^2}{\partial y_i\partial y_j}\left(\frac{1-ik_0r}{r^3}\right)e^{ik_0r}+\frac{\partial}{\partial y_i}\left(\frac{1-ik_0r}{r^3}\right)\frac{\partial}{\partial y_j}\left(e^{ik_0r}\right) \\ &+\frac{\partial}{\partial y_j}\left(\frac{1-ik_0r}{r^3}\right)\frac{\partial}{\partial y_i}\left(e^{ik_0r}\right)+\left(\frac{1-ik_0r}{r^3}\right)\frac{\partial^2}{\partial y_i\partial y_j}\left(e^{ik_0r}\right),\end{aligned} \tag{C.8}$$

and with

$$\frac{\partial^2}{\partial y_i\partial y_j}\left(\frac{1-ik_0r}{r^3}\right)=\frac{5r_ir_j-\delta_{ij}r^2}{r^7}(3-2ik_0r)+2ik_0\frac{r_ir_j}{r^6}, \tag{C.9}$$

$$\frac{\partial^2}{\partial y_i\partial y_j}\left(e^{ik_0r}\right)=\frac{ik_0(\delta_{ij}r^2-r_ir_j)-k_0^2r_ir_jr}{r^3}e^{ik_0r}. \tag{C.10}$$

References

[1] M.J. Lighthill, On sound generated aerodynamically. I. General theory, Proc. R. Soc. Lond. Ser. A, Math. Phys. Sci. 211 (1952) 564–587.
[2] P.E. Doak, L. Rosenhead, Acoustic radiation from a turbulent fluid containing foreign bodies, Proc. R. Soc. Lond. Ser. A, Math. Phys. Sci. 254 (1276) (1960) 129–146.
[3] D.G. Crighton, F.G. Leppington, On the scattering of aerodynamic noise, J. Fluid Mech. 46 (3) (1971) 577–597.
[4] J.E. Ffowcs Williams, L.H. Hall, Aerodynamic sound generation by turbulent flow in the vicinity of a scattering half plane, J. Fluid Mech. 40 (1970) 657–670.
[5] W. Devenport, N. Alexander, S. Glegg, M. Wang, The sound of flow over rigid walls, Annu. Rev. Fluid Mech. 50 (2018).
[6] M.S. Howe, On the generation of sound by turbulent boundary layer flow over a rough wall, Proc. R. Soc. Lond. Ser. A, Math. Phys. Sci. 395 (180) (1984) 247–263.
[7] B. Boley, A method for the construction of Green's functions, Q. Appl. Math. 3 (14) (1956) 249–257.
[8] J. Ostertag, S. Guidati, G. Guidati, S. Wagner, A. Wilde, N. Kalitzin, Prediction and measurement of airframe noise on a generic body, in: 6th Aeroacoustics Conference and Exhibit, 2000.
[9] F. Hu, Y. Guo, A. Jones, On the computation and application of exact Green's function in acoustic analogy, in: 11th AIAA/CEAS Aeroacoustics Conference, 2005.
[10] T. Takaishi, M. Miyazawa, C. Kato, A computational method of evaluating noncompact sound based on vortex sound theory, J. Acoust. Soc. Am. 121 (3) (2007) 1353–1361.
[11] S. Glegg, W. Devenport, Aeroacoustics of Low Mach Number Flows: Fundamentals, Analysis, and Measurement, Academic Press, 2017.
[12] P.A. Martin, Multiple Scattering: Interaction of Time-Harmonic Waves with N Obstacles, vol. 107, Cambridge University Press, 2006.
[13] J.C. Nédélec, Acoustic and Electromagnetic Equations: Integral Representations for Harmonic Problems, Springer Science & Business Media, 2001.
[14] E. Darve, The fast multipole method: numerical implementation, J. Comput. Phys. 160 (1) (2000) 195–240.
[15] W. Hackbusch, A sparse matrix arithmetic based on $\mathcal{H}$-matrices. Part I: introduction to $\mathcal{H}$-matrices, Computing 62 (2) (1999) 89–108.
[16] M. Bonnet, Boundary Integral Equations Methods in Solids and Fluids, John Wiley and Sons, 1999.
[17] S. Chaillat, M. Bonnet, J.-F. Semblat, A multi-level fast multipole BEM for 3-D elastodynamics in the frequency domain, Comput. Methods Appl. Mech. Eng. 197 (2008) 4233–4249.
[18] S. Chaillat, L. Desiderio, P. Ciarlet, Theory and implementation of $\mathcal{H}$-matrix based iterative and direct solvers for Helmholtz and elastodynamic oscillatory kernels, J. Comput. Phys. 351 (2017) 165–186.
[19] S. Börm, L. Grasedyck, W. Hackbusch, Introduction to hierarchical matrices with applications, Eng. Anal. Bound. Elem. 27 (5) (2003) 405–422.
[20] H.G. Davies, The radiated fields of multipole point sources near a solid spherical surface, J. Fluid Mech. 43 (3) (1970) 597–606.
[21] X. Gloerfelt, F. Pérot, C. Bailly, D. Juvé, Flow-induced cylinder noise formulated as a diffraction problem for low Mach numbers, J. Sound Vib. 287 (1–2) (2005) 129–151.
[22] M.S. Howe, Theory of Vortex Sound 33, Cambridge University Press, 2003.
[23] J.R. Mathews, N. Peake, An analytically-based method for predicting the noise generated by the interaction between turbulence and a serrated leading edge, J. Sound Vib. 422 (2018) 506–525.
[24] M.S. Howe, Edge-source acoustic Green's function for an airfoil of arbitrary chord, with application to trailing edge noise, Q. J. Mech. Appl. Math. 54 (1) (2001) 139–155.
[25] L. Hörmander, The Analysis of Linear Partial Differential Operators I: Distribution Theory and Fourier Analysis, Springer, 2015.